A case study of dynamic triggering in the Kiskatinaw area of the Montney Formation, British Columbia

Brindley Smith, Department of Earth and Planetary Sciences
McGill University, Montreal

December, 2020

A thesis submitted to McGill University in partial fulfillment of the requirements of the degree of

Master of Science

Abstract

In this study I investigate the potential occurrence of remote dynamic triggering in the Kiskatinaw area of British Columbia, Canada, over a 30-month time interval following the installation of the McGill seismic network. I use visual waveform analysis, as well as a multi-station matched filter catalogue enhancement method, to detect any remotely triggered earthquakes. Potentially-triggering mainshocks are required to surpass a measured peak ground velocity of 100 μm/s, surface wave magnitude ≥ 6, and have depths ≤ 100 km. The visual analysis method reveals triggered events buried within the teleseismic surface waves of two mainshocks, as well as events up to 4 hours after a mainshock's first arrival. Following the catalogue enhancement for 5 days before and after each candidate mainshock, I use a combination of the P, γ, β, and Z statistical tests to confirm that seismicity rate increases are significant enough to indicate triggering. I find multiple mainshocks with statistically-significant triggering, each of which with depths < 35 km and measured peak dynamic triggering stresses from 5-16 kPa. I also observe transient stresses responsible for directly triggering events down to 0.05 kPa, implying that the responsive faults are critically-stressed, and have a triggering threshold lower than previously observed in this region. Two of the triggering mainshocks are not associated with injection activity in the 10-day catalogue enhancement periods, indicating that pore pressures may have remained high in the region for days or weeks after injection has ceased.

Résumé

Dans cette étude, j'étudie l'occurrence potentielle d'un déclenchement dynamique à distance dans la région de Kiskatinaw en Colombie-Britannique, au Canada, dans les 30 mois suivant l'installation du réseau sismique de McGill. J'utilise l'analyse visuelle des ondes, ainsi qu'une méthode d'amélioration du catalogue: un filtre jumelé à multiple stations, pour détecter tous les tremblement de terre déclenché à distance. Pour que des chocs principaux soivent potentiellement déclencheurs, ils doivent dépasser une vitesse maximale du sol de 100 μm/s, une magnitude d'onde de surface de 6, et avoir des profondeurs $\leq$ 100 km. L'analyse visuelle révèle des événements déclenchés enfouis dans les ondes de surface télésismiques de deux chocs principaux, ainsi que des événements jusqu'à 4 heures après la première arrivée d'une secousse principale. Suite à l'amélioration du catalogue pendant 5 jours avant et après chaque choc principal candidat, j'utilise une combinaison des tests statistiques P, γ, β et Z pour confirmer que les augmentations du taux de sismicité sont suffisamment importantes pour indiquent le déclenchement. Je trouve plusieurs événements avec un déclenchement statistiquement significatif, chacun avec des profondeurs $<$ 35 km et des contraintes de déclenchement dynamiques de pointe mesurées de 5 à 16 kPa. J'observe également des contraintes transitoires responsables du déclenchement direct d'événements jusqu'à 0.05 kPa, ce qui implique que de nombreuses failles locales sont soumises à des contraintes critiques, et ont un seuil de déclenchement inférieur à celui observé précédemment dans cette région. Deux des chocs principaux de déclenchement ne sont pas associés à l'activité d'injection au cours des périodes d'amélioration du catalogue de 10 jours, ce qui indique que les pressions interstitielles peuvent être restées élevées dans la région pendant des jours ou des semaines après la fin de l'injection.

Acknowledgements

First and foremost I would like to thank my supervisor Yajing Liu for her guidance and patience in helping me complete my thesis project. Her work ethic and passion for the sciences were a wonderful motivation in finishing this work to the best of my abilities, and I greatly appreciate her giving me this opportunity. I would also like to thank my friends and colleagues from our seismology team at McGill: Andres Peña Castro, John Onwuemeka, Ge Li, Lise Alalouf-Schmitt, Julia Morales-Aguirre, Alessandro Verdecchia, and Ruhollah Keshvardoost for their support and advice despite often being very busy themselves. Andres helped me establish codes for the peak ground velocity calculations, multi-station matched-filter, and spectral analysis. John and Ge also helped me with a wide variety of coding and debugging issues that I came across during my time at McGill as well. I would also like to thank my colleagues from the seismology team in Bochum, Germany for their advice and cooperation. Marco Roth downloaded the well data from the BC Oil and Gas Commission, and provided useful advice for the implementation of $NonLinLoc$. He and Kilian Kenma processed the catalogue enhancement for the 3 datasets with the largest number of templates using the servers at Ruhr University. I would also like to acknowledge Bei Wang for his initial advice for the project, as well as completing its predecessor. I met many other brilliant students at McGill University, and I would like to thank them for making the experience more enjoyable, particularly my friends Emily Mick, Jessica Salas-Navarro, David Martineau, Florentine Zwillich, Caroline Studnicky, Debarati Das, Robert Collar, Leah Mindorff, and Kristyn Rodzinyak for helping get me through the tough patches of my research. Lastly, I would like to thank my parents for their unending support in finishing my thesis, and especially my partner of nearly 10 years, Ashley Mowat, who not only moved across the country to support me, but has backed me every step of the way. I wouldn't be here without her.

Table of Contents

List of Figures

List of Tables

Chapter 1

1 Introduction

1.1 Motivation for the project

Earthquakes are a naturally occurring process that result from the rupture and slip along critically-stressed faults. While earthquakes are typically found along plate boundaries, they can also be located in intraplate regions with relatively low tectonic strain rates (Ellsworth, 2013; Kao et al., 2018a; McGarr et al., 2002). The recent development of hydraulic fracturing (fracking) and wastewater disposal for shale gas production in the Western Canada Sedimentary Basin (WCSB), an intraplate region with historically low background seismicity, has led to a large increase in earthquakes caused by human activity, also known as induced seismicity (Farahbod et al., 2015; Grigoli et al., 2017; Schultz et al., 2015). Previous studies have suggested that areas with injection-related seismicity may also be more susceptible to earthquakes caused by dynamic triggering, which can imply that a region is critically stressed (van der Elst and Brodsky, 2010; van der Elst et al., 2013; Wang et al., 2019, 2015). Remote dynamic triggering occurs due to the arrival of transient stresses from large, distant earthquakes temporarily altering the stress field in a region and promoting fault slip (Hill and Prejean, 2015). To mitigate seismic hazard and induced seismicity, it is essential to improve our understanding of induced seismicity and dynamic triggering.

1.2 Induced seismicity

Induced seismicity can be caused by a variety of processes, such as nuclear tests, hydro dams, mine blasting activity, fracking, and wastewater injection (Grigoli et al., 2017; McGarr et al., 2002). Canada's WCSB in particular has seen a significant increase in induced seismicity relative to historic levels due to modern fracking and wastewater injection processes (Atkinson et al., 2016). This increase over time is shown in Figure 1.1, where I plot annual seismicity recorded by Natural Resources Canada (NRCan) since it's implementation in 1985. The typically accepted mechanism for induced events in this region is brittle failure along faults in or around the tight shale formations as a result of increased pore pressure from injected fluids (Healy et al., 1970; Pearson, 1981; Schultz et al., 2018). Induced earthquakes in the WCSB are typically small ($M < 3$), but can exceed M_W 4, implying that there is a significant potential seismic hazard for infrastructure, which eventually led to the implementation of a traffic light protocol (Kao et al., 2018b; Wang et al., 2017). While induced seismicity in the WCSB is almost exclusively associated with injection activity, not all of this activity actually results in detectable earthquakes, and a combination of high injection volumes and relatively high tectonic strain rates lead to the highest chance of induced seismicity occurring (Kao et al., 2018a). The Kiskatinaw area (KKTA), British Columbia, is located within a region of moderately high background strain rates in the WCSB, and along with its frequent induced seismicity, has clear evidence of critically-stressed subsurface faults (Kao et al., 2018a; Visser et al., 2017, 2020; Wang et al., 2019).

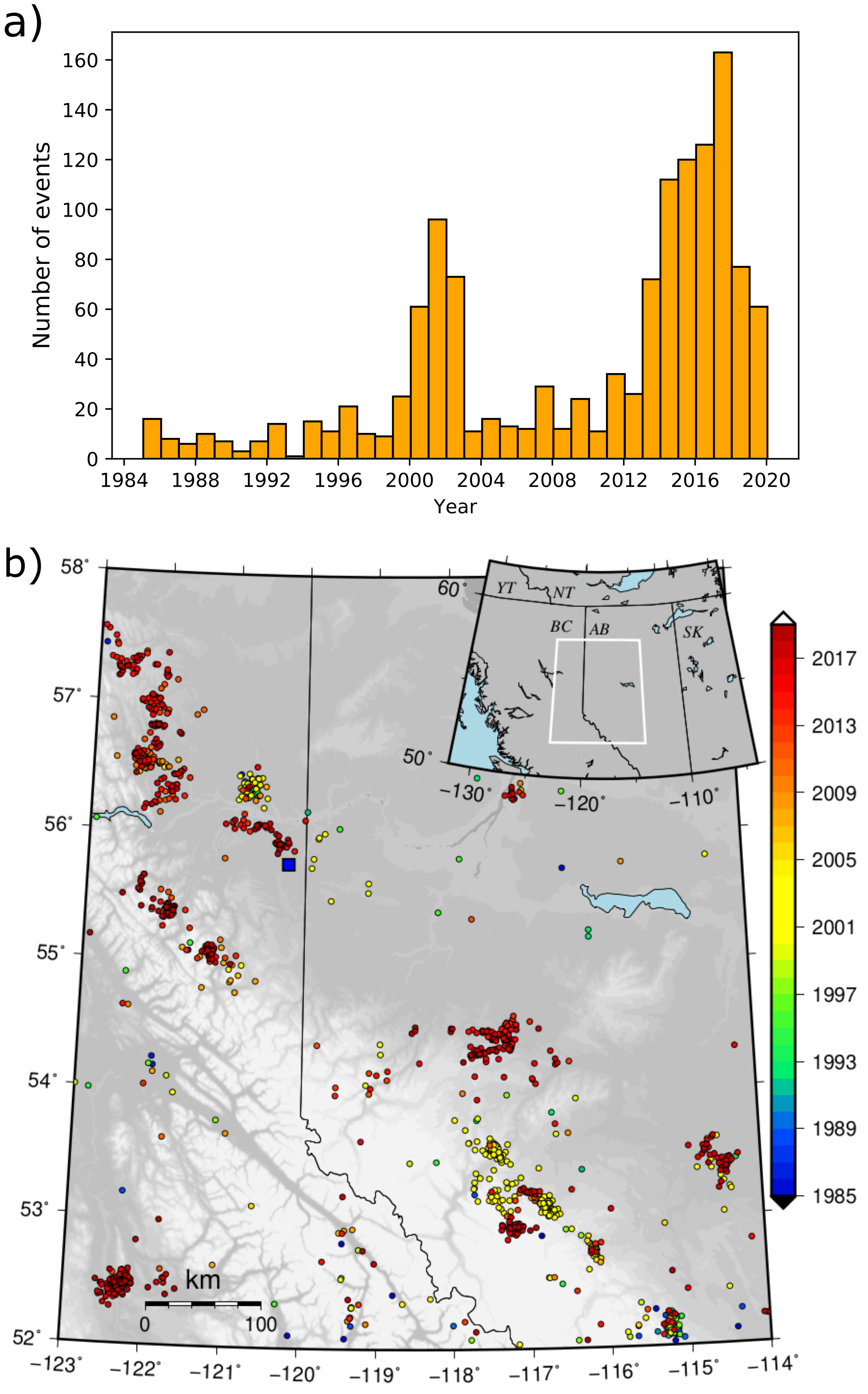

Figure 1.1: a) Annual seismicity in the Western Canadian Sedimentary Basin (WCSB) from 1985 until 2020 for events with $M_L \geq 2.5$, from the Natural Resources Canada catalogue. Earthquakes were collected within 52 to 58 Latitude and -123 to -114 Longitude to approximate the WCSB region. b) As above, with circles to represent events, coloured by year, and Dawson Creek as a blue square. Provincial boundaries are denoted by black lines, and the map area is outlined by a white box in the inset map.

1.3 Dynamic earthquake triggering

Earthquake triggering refers to the natural process by which a stressed fault can be forced above its rupture threshold by an external source, resulting in slip along the fault and subsequent earthquake. Remote dynamic triggering is the process in which the teleseismic waves from a large, distant earthquake can cause a temporary oscillation in the stress field of a local area (Aki and Richards, 2002; Hill and Prejean, 2015). These triggering earthquakes can be located hundreds or thousands of kilometres away from the region experiencing an increase in seismicity, due to the surface wave energy decreasing slowly with distance (Hill et al., 1993; Velasco et al., 2008). Aside from distance, a range of factors can influence the potential for a large mainshock to dynamically trigger earthquakes, such as its magnitude, depth, rupture directivity, and the extent of low-frequency surface wave shaking (Brodsky and Prejean, 2005; Gomberg et al., 2001; Hough and Kanamori, 2002).

Evidence of dynamic triggering is typically found either through the detection of small earthquakes buried within the surface wave train of the teleseismic waves (Velasco et al., 2008), or represented by an increase in the seismicity rate over a given time range in a given region. This seismicity increase is generally confirmed through the use of statistical tests, and can be delayed by a matter of hours or even days (Gomberg et al., 2001; Marsan and Wyss, 2011; Prejean et al., 2004). The prediction of the required peak dynamic stress that can trigger seismicity has been an ongoing point of study, and has been shown to fall as low as $\sim$ 0.1 kPa (Brodsky and Prejean, 2005; Cochran et al., 2004; van der Elst and Brodsky, 2010; Wang et al., 2015). In the WCSB, previous studies have observed transient stresses capable of triggering earthquakes as low as 0.16-1.7 kPa (Wang et al., 2019, 2015).

1.4 The importance of the new, dense seismic network

Studies in seismology tend to utilize whatever information is available at the time; in most cases being dependent on the density and quality of seismic stations in a network for any given region (Schultz et al., 2015; Visser et al., 2017). The KKTA has been an important area regarding studies on induced seismicity, including recent studies on remote dynamic triggering that included this locality (Wang et al., 2019, 2015). The main limitations of studies on induced seismicity tend to arise due to the prevalence of very small earthquakes, with magnitudes even falling below 0 (Roth et al., 2020; Visser et al., 2017, 2020), and the difficulties involved in locating them. Two permanent stations of the CN network were present in the KKTA as of 2014. In July 2017, the McGill seismology team installed a network of temporary broadband seismometers in the KKTA, which immediately led to an increase in the ability to detect microseismicity, and more than 5000 induced events were located in a 6 month period following station installation (Visser et al., 2020). The station density was improved further with additional installations for the XL and 1E networks from 2018 through 2020 (Table A.1), as well as the installation of the EO network by the University of Calgary in 2020. The distribution of stations used in this study are shown in Figure 1.2. With these additional stations, it is much easier to detect the microseismicity commonly associated with fluid injection activity, as well as events that may arise due to remote dynamic triggering.

1.5 Goals of this project

In this study, I will attempt to observe cases of remote dynamic triggering in the KKTA with the aid of a dense seismic network and multi-station matched filter approach. With more stations in the KKTA, there is a greater probability of being able to find the small events associated with induced seismicity and dynamic triggering that would otherwise be missed. In previous studies, triggering stresses in the WCSB were found to fall as low

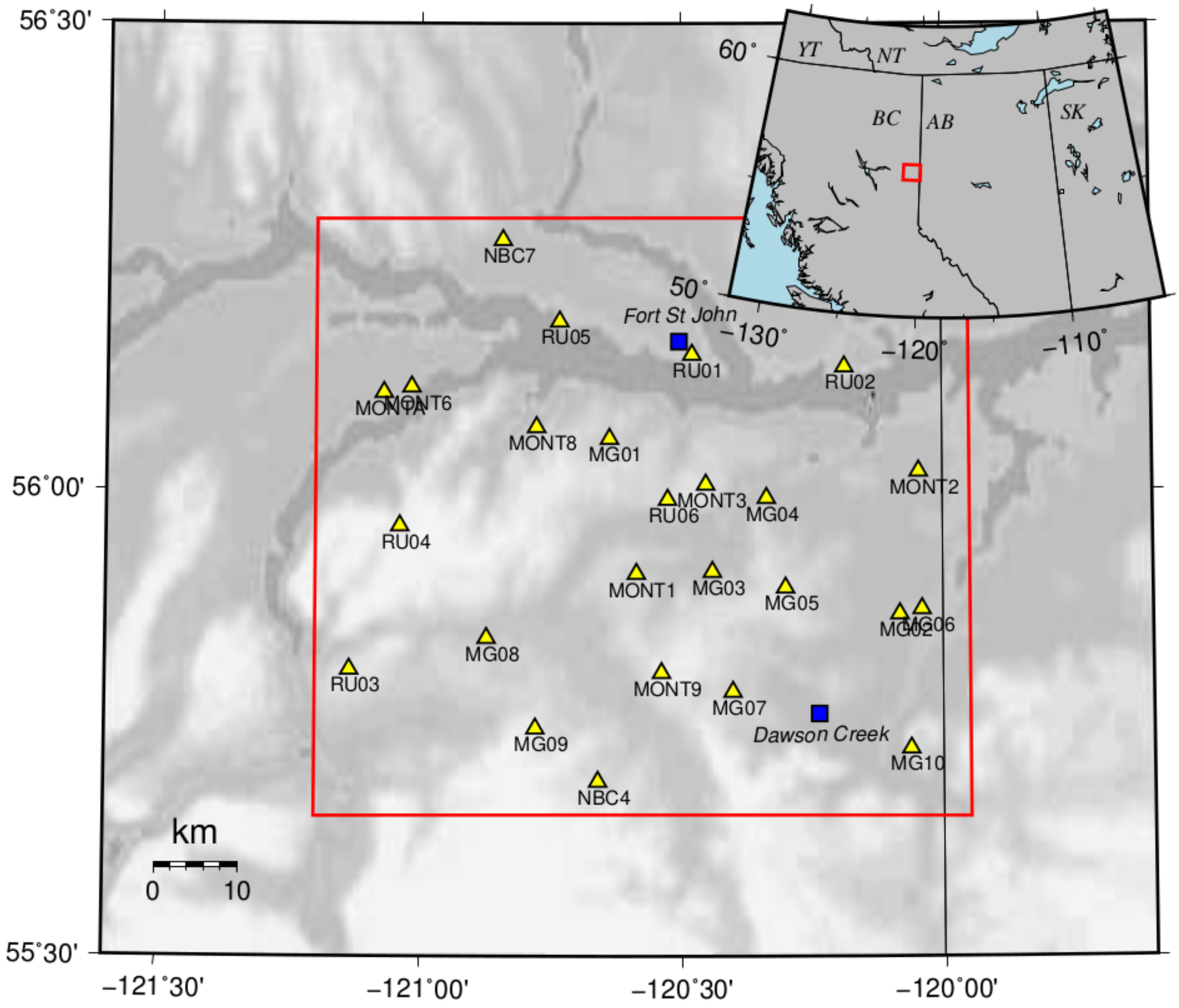

Figure 1.2: Map showing the study area (red box) in the Kiskatinaw region of the Western Canadian Sedimentary Basin. Stations used in this study are shown as yellow triangles, with Dawson Creek and Fort St John denoted by blue squares, and provincial boundaries as black lines. The inset shows the location of the study area in western Canada.

as 0.16-1.7 kPa but, despite this, only a portion of the studied mainshocks had been observed to result in dynamic triggering (Wang et al., 2019, 2015). While this threshold is roughly equivalent to the magnitude of solid-earth tidal stresses (up to 5 kPa), it remains unclear whether there is ubiquitous correlation between seismicity rate change and solid earth tides (Beeler and Lockner, 2003; Cochran et al., 2004). It is possible that with more rigorous enhancement processes, statistical tests, and station usage that I may be able to determine if a higher number of — if not all — large distant events above a certain dynamic stress threshold are capable of triggering earthquakes in a particularly stressed region such as the KKTA. It may also be possible to detect a lower triggering threshold for transient stresses than the previously determined threshold of 0.16 kPa in this region (Wang et al., 2015).

I define a set of criteria for selecting potential triggering mainshocks for a time period starting August 2017, the point at which the XL network had been established, and continuing through January 2020. Once selected, I visually analyze the waveforms around each of the candidate triggering mainshocks to determine if direct triggering has occurred. I then test a variety of threshold parameters for catalogue enhancement to determine the optimal settings, confirm their reliability, and apply the enhancement to a 10-day time span around each mainshock event. I use the catalogue recently published by Roth et al. (2020), for a study area outlined in Figure 1.2. I will also show a comparison of any detected events with nearby injection activity, to see how much of an effect it has on the seismic activity. To confirm if any changes in seismicity rates are statistically significant, I perform a series of statistical tests for the datasets around each mainshock. As a final test to examine the potential effects of the frequency of surface wave shaking on potential dynamic triggering, I perform a spectral analysis of each event.

Chapter 2

2 Selection of triggering mainshocks and direct triggering

2.1 Selection of triggering mainshocks

For the best chances of observing remote dynamic triggering, I outline a set of criteria the teleseismic events must fit in order to be considered as candidate triggering mainshock events. I first perform a search of the Global Centroid-Moment-Tensor (GCMT) catalogue (Dziewonski et al., 1981; Ekström et al., 2012) for events with surface wave magnitudes (M_S) $\geq$ 6.0 and depths $\leq$ 100 km following activation of the McGill seismic network, for a time span of August 2017 through January 2020. The surface wave magnitude threshold was selected to focus on the large earthquakes that result in higher peak ground velocity (PGV) levels in the study area, which may lead to the strong surface-wave shaking required for dynamic triggering to occur (Brodsky et al., 2000; Hill et al., 1993). The depth threshold was chosen because shallow earthquakes are often associated with increased surface wave energy (Aki and Richards, 2002; Gomberg et al., 2001).

The above criteria, as well as a final requirement for PGV to surpass a given threshold, have been used in previous studies to refine the earthquake selection process (Peña Castro et al., 2019; Wang et al., 2019, 2015). While there has been a variety of previously-established triggering thresholds (Brodsky and Prejean, 2005; Cochran et al., 2004; van der Elst and Brodsky, 2010; Wang et al., 2015), I require a PGV $\geq$ 100 μm/s because it has already been demonstrated as sufficient for dynamic triggering in the WCSB (Wang et al., 2019). The PGV calculation occurs in 2 parts. I initially estimate the theoretical peak ground velocity (PGV$_t$) to further narrow down the candidate dataset, followed by calculating the measured peak ground velocity (PGV$_m$) for three components of each broadband station. By using the PGV$_m$ I can better account for factors such as the ray path and directivity of seismic energy, which can result in deviations from PGV$_t$ estimates.

2.2 Peak ground velocity calculations

To calculate the PGV$_t$, I first need to determine the source-receiver distance. To do this I use data from the GCMT catalogue for event locations, along with station data in the KKTA downloaded from the Incorporated Research Institutions for Seismology (IRIS) archives (Table A.1, Figure 1.2). Source-receiver distance is calculated using the Vincenty Inversion Solution on the WGS94 ellipsoid (Vincenty, 1975). I then calculate the PGV$_t$ at station MG05 of the XL network for each earthquake. I use MG05 for these calculations because it had the second highest number of phase picks in a manually-picked earthquake catalogue featuring the updated KKTA seismic network, as well as one of the lowest magnitude correction factors (Visser et al., 2020), indicating that it is in an ideal location and has a good signal.

The PGV$_t$ was calculated using an empirical ground motion regression (Lay and Wallace, 1995; van der Elst and Brodsky, 2010; Velasco et al., 2004):

$$M_S = logA_{20} + 1.66log\Delta + 2.0, \tag{2.1}$$

$$PGV \approx \frac{2\pi A_{20}}{T}, \tag{2.2}$$

where A_{20} is the amplitude (in μm) of surface waves with a period (T) of 20s, and Δ is the epicentral source-receiver distance in degrees. A 20s period is utilized to focus on the energy imparted by low frequency surface waves (Aki and Richards, 2002), which are considered to be more effective at triggering seismicity than energy concentrated at higher frequencies (Brodsky and Prejean, 2005; Wang et al., 2019). To ensure I only measure amplitude for low frequency energy, I use a low-pass filter of 0.05 Hz.

The GCMT earthquake search resulted in 267 events for the August 2017 - January 2020 period. After calculating the PGV_t values for the KKTA, I was left with 14 potential triggering teleseismic events above the 100 μm/s threshold (Figure 2.1, Table 2.1). The distance of these events to station MG05 ranged from 8 - 47.6 degrees, and candidate mainshock magnitudes fell within M_S 6 - 8.2 (Figure 2.1). The PGV_t of two of these events was 99 μm/s, but they were included for completeness as their USGS locations resulted in PGV_t estimates of 104 μm/s (`https://osf.io/qsxhj/`).

To calculate the PGV_m, I first organize the waveform data by mainshock date and split it into separate daily directories. Instrument response is then removed using the station response files extracted from IRIS, and the horizontal channels are rotated to align with the radial and transverse components of incoming waves. By rotating the horizontal components from North and East, the amplitudes of incoming Rayleigh and Love Waves are maximized. The first arrival of the P wave of each mainshock is calculated using the Preliminary Reference Earth Model in TauP (Crotwell et al., 1999; Dziewonski and Anderson, 1981). To determine the PGV_m, I select the point of highest amplitude based on the arrival time of surface waves travelling between 4.4 to 2.0 km/s, to capture the time where surface wave energy is most likely concentrated for each of the vertical and two rotated horizontal channels (Telford et al., 1990). I require at least one of the PGV_m values from the radial (PGV_R), transverse (PGV_T), or vertical (PGV_Z) components to surpass the PGV_t threshold. I also calculate the peak dynamic triggering stress (τ, in kPa) for the

Table 2.1: Earthquakes with theoretical peak ground velocity (PGV$_t$) >100 μm/s. Each candidate triggering mainshock is numbered in chronological order, with origin time in UTC with locations from the Global Centroid-Moment-Tensor catalogue. Source-receiver distance and theoretical peak ground velocity are calculated for station MG05. *Mainshocks 11 and 12 are included due to their locations in the USGS catalogue resulting in PGV$_t$ estimates of 104 μm/s.

Event ID	Date	Origin time	Lat	Long	Depth (km)	Mag (M$_S$)	Distance (deg)	PGV$_t$ (μm/s)
1	2017-09-08	04:49:19	15.38	-93.66	44.8	8.2	45.01	897
2	2018-01-10	02:51:33	17.56	-83.86	16.5	7.5	47.17	166
3	2018-01-23	09:31:40	56.22	-149.12	33.6	7.9	15.98	2508
4	2018-10-22	05:39:39	48.95	-129.54	15.2	6.5	8.92	262
5	2018-10-22	06:16:26	49.14	-129.89	16.1	6.8	8.91	525
6	2018-10-22	06:22:48	49.00	-130.13	15.2	6.5	9.11	253
7	2018-11-30	17:29:29	61.49	-150.02	48.2	7	16.25	307
8	2018-12-20	17:01:55	54.94	164.75	17.1	7.3	40.41	135
9	2019-07-04	04:30:44	51.16	-130.64	12	6.2	7.74	166
10	2019-07-06	03:19:53	35.78	-117.58	12	7.1	20.20	269
11	2019-12-23	19:49:43	50.48	-130.18	12	6	8.03	99*
12	2019-12-23	20:56:23	50.29	-129.91	12	6	8.01	99*
13	2019-12-25	03:36:01	50.41	-130.22	14.9	6.3	8.08	195
14	2020-01-28	19:10:24	19.33	-79.55	23.9	7.7	47.55	259

highest component of each event by converting the particle motion at this point using another equation (Love, 1927):

$$\tau = \frac{PGV \times \mu}{V_R}, \tag{2.3}$$

in which the shear modulus (μ) is assumed to be 32 GPa for continental crust, and a Raleigh-wave velocity (V_R) of 2.85 km/s, as defined by previous work in this region (Wang et al., 2019). To confirm that the PGV$_m$ calculation results would not vary sig-

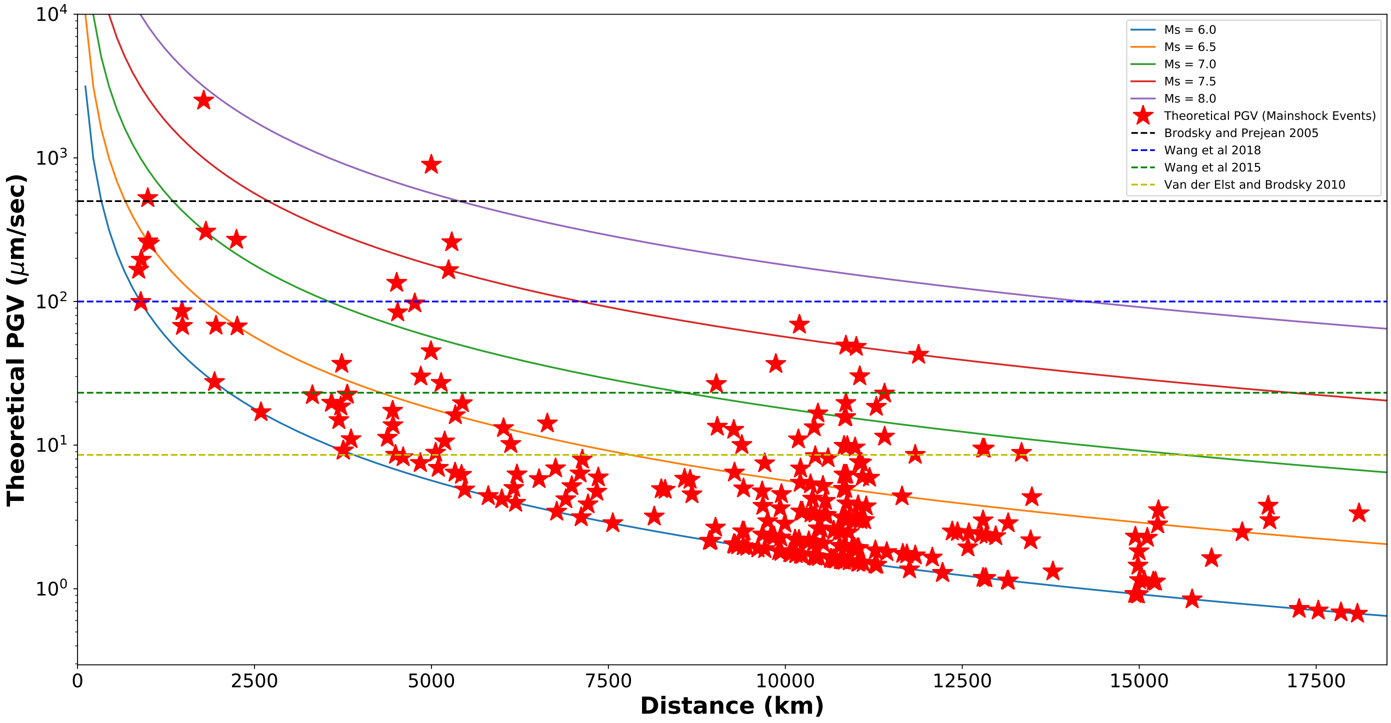

Figure 2.1: Theoretical peak ground velocity (PGV$_t$) results for earthquakes from the Global Centroid-Moment-Tensor catalogue. Solid curved lines show PGV$_t$ estimates as a function of distance over a range of magnitudes, calculated using the empirical ground motion regression (Equations 2.1, 2.2). Each red star represents an earthquake. Horizontal dashed lines represent established triggering thresholds from previous studies. Source receiver distance is calculated relative to station MG05.

nificantly between stations in the KKTA, I also calculate them for station NBC4 of the CN network.

A total of 9 of the 14 mainshocks had PGV$_m$ values above the 100 μm/s threshold (Figure 2.2, Table 2.2). PGV values between individual components varied by up to an order of magnitude for each event, and PGV$_m$ results for events within 2000 km of the reference station all fell below the PGV$_t$ estimates. All 5 of the candidate mainshocks that did not pass the PGV$_m$ threshold were located within 1000 km of the reference station, implying that event magnitude is more important than source-receiver distance (Figure 2.2, Table 2.2). In all but one of the accepted candidate mainshocks, PGV$_T$ was the highest of the three measured components, and τ ranged from 1.74 to 16.12 kPa. The PGV$_m$ did not vary significantly when compared with those of station NBC4, with the largest difference being from Mainshock 1 having a τ ~3 kPa lower than its MG05 counterpart (Table A.2). The locations and focal mechanism solutions, which mostly indicate strike-slip behaviour, of the accepted candidate mainshock events are shown in Figure 2.3.

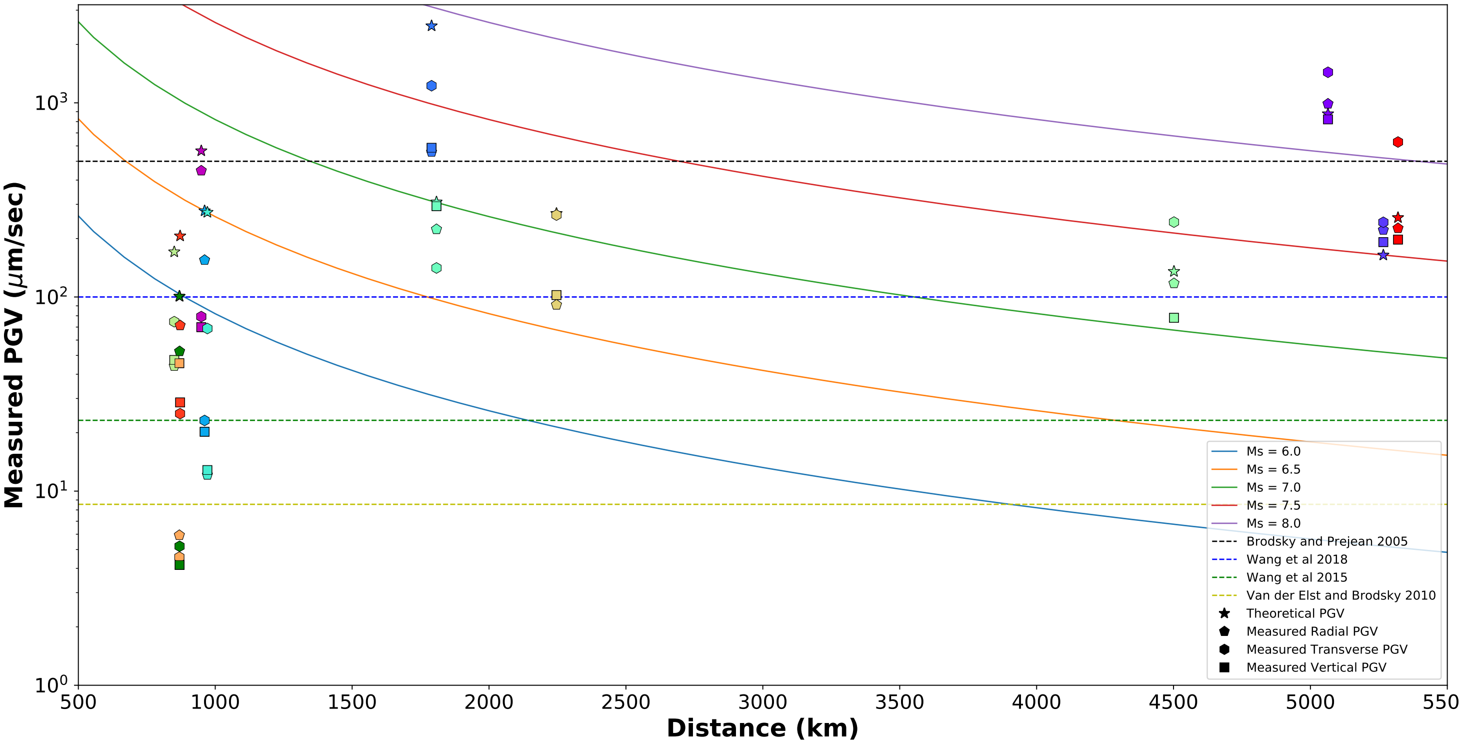

Figure 2.2: Measured peak ground velocity (PGV$_m$) results for earthquakes with theoretical peak ground velocity (PGV$_t$) values >100 μm/s. The solid curves show PGV$_m$ for the radial (pentagons), transverse (hexes), and vertical (squares) component of each event as a function of distance over a range of magnitudes, calculated using the empirical ground motion regression (equation 2.2). Stars denote the PGV$_t$ values for each earthquake, and horizontal dashed lines represent established triggering thresholds from previous studies. Each colour represents the results for one mainshock, with source-receiver distances indicated by Table 2.1.

Table 2.2: Earthquakes with measured peak ground velocities >100 μm/s for at least one of the radial (PGV_R), transverse (PGV_T), or vertical (PGV_Z) components of station MG05. Event ID is tied to those of Table 2.1, with event origin times in UTC. Peak dynamic triggering stress (τ) is calculated from the component of highest measured peak ground velocity, and PGV_t is the theoretical peak ground velocity, for each event. Source area represents the approximate epicentral location.

Event ID	Date	Origin time	Mag (M_W)	PGV_R (μm/s)	PGV_T (μm/s)	PGV_Z (μm/s)	PGV_t (μm/s)	τ (kPa)	Source area
1	2017-09-08	04:49:19	8.2	989	1437	822	897	16.13	Mexico
2	2018-01-10	02:51:33	7.5	221	243	192	166	2.72	Honduras
3	2018-01-23	09:31:40	7.9	558	1225	587	2508	13.75	Alaska
4	2018-10-22	05:39:39	6.5	20	155	23	262	1.74	Port Hardy
5	2018-10-22	06:16:26	6.8	70	447	79	525	5.02	Port Hardy
7	2018-11-30	17:29:29	7.1	223	141	294	307	3.30	Alaska
8	2018-12-20	17:01:55	7.2	118	243	78	135	2.73	Russia
10	2019-07-06	03:19:53	7	91	264	102	269	2.96	California
14	2020-01-28	19:10:24	7.7	226	628	198	259	7.05	Cuba

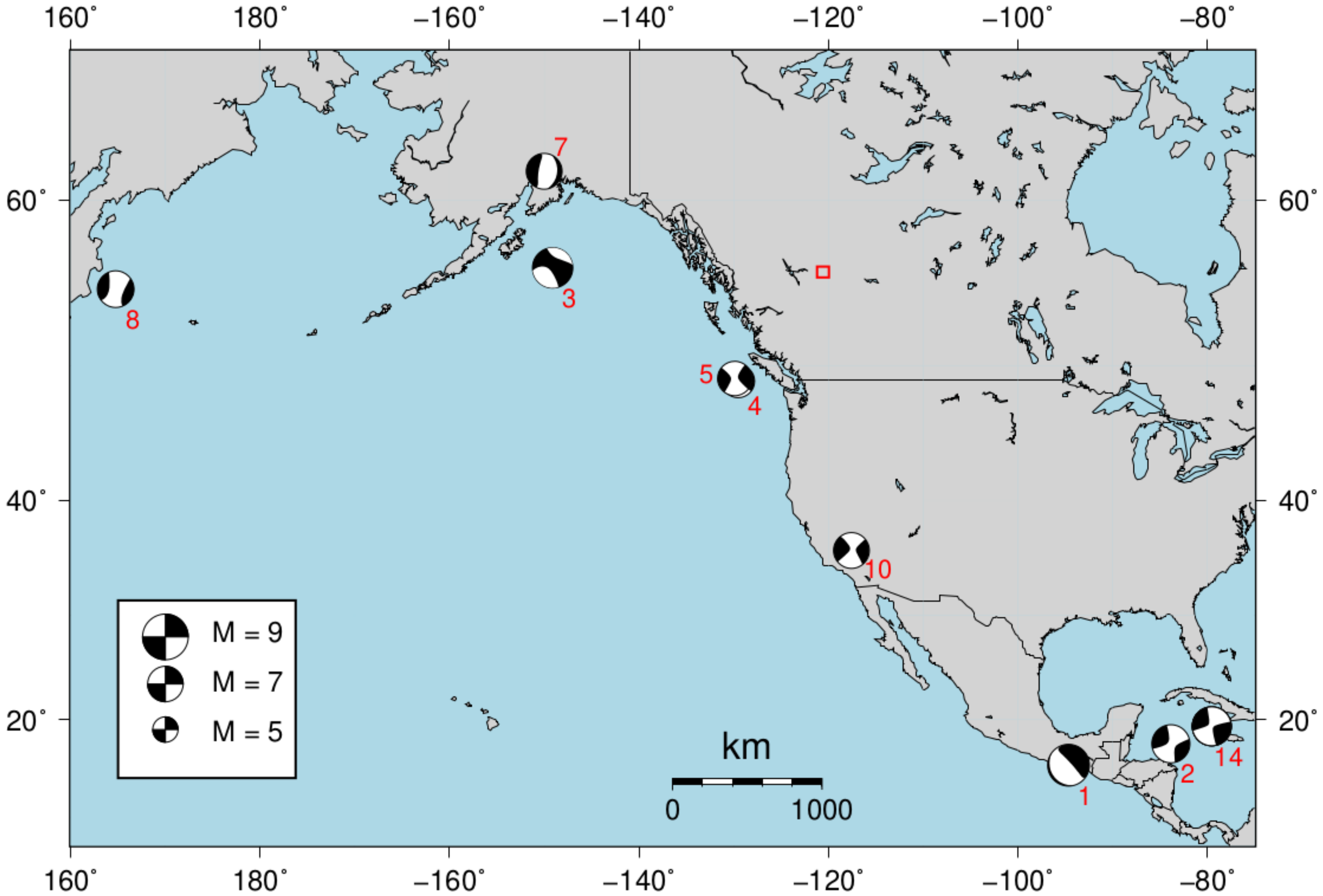

Figure 2.3: Focal mechanisms for earthquakes that passed candidate mainshock selection criteria, numbered by Event ID (see Table 2.2). The study area is shown as a red box.

2.3 Visual analysis method

With the potentially-triggering mainshocks identified, I can then begin looking for dynamically-triggered earthquakes. The first method I use for this is a visual waveform analysis to find any triggered events buried within the surface wave train and coda. Due to triggered events being very small relative to the incoming teleseismic surface wave energy, I search for them using a 5 Hz high-pass filter (Velasco et al., 2008; Wang et al., 2019). Since small events are usually associated with high frequency energy, this filter should allow me to visualize these events over the low frequency energy. I use pyrocko's snuffler software package for waveform analysis, with a 30 second time window and narrowing frequencies, when necessary, to a bandpass of 8-30 Hz to better visualize potential events (Pyrocko, 2018). For an event to be considered a real earthquake, I need to see clear P and S phase arrivals on at least one station. If any triggered events are observed in the surface wave train, I extend the analysis to 4 hours before and after the mainshock's first arrival time. By doing this I can see if there are any immediate changes in the seismicity rate following the mainshock's arrival if background seismicity was present.

Two mainshocks were found to have evidence of direct dynamic triggering through the waveform analysis. Originating west of Vancouver Island, Mainshock 5 triggered an earthquake at approximately 6:22:12 am (UTC). This triggered event was difficult to identify on the waveform, as it only becomes clearly visible in a narrow bandpass of approximately 5-10 Hz (Figure 2.4), and was the only event located within the 8 hr time window around the two temporally-adjacent candidate mainshocks on that day. Its origin time did, however, coincide with the peak of low frequency surface wave energy (Figure 2.4). The second mainshock responsible for directly triggered events, Mainshock 14 (near Cuba), had far more seismicity following the arrival of the teleseismic waves. There were 2 events before the mainshock's arrival, and 18 afterwards (Figure 2.5, Table A.3). Of note for some of these events is their significant time lag following the mainshock, with many being delayed by 60-150 minutes after the first arrival, where the surface waves have already appeared to decrease towards background levels. I estimated the R2 and R3 surface wave arrivals, assuming a velocity of 4.4 km/s, to observe if they could be correlated with triggered events in this dataset. There appears to be no increase in the energy level following their estimated arrivals, although 3 events did occur shortly following the estimated R2 arrival (Figure 2.5).

I calculate the transient triggering stresses (τ_t) responsible for each of the directly triggered events within the surface wave trains of mainshocks 5 and 14. To do this I take the peak amplitude from the highest station component (PGV$_R$, PGV$_T$, or PGV$_Z$) following a low-pass filter of 0.05 Hz, and within a range of 10 seconds before to 5 seconds after each triggered event's first arrival, then calculate τ_t using equation 2.3. The triggered event within the surface wave train of mainshock 5 had a τ_t of 0.89 kPa. In order of occurrence, the τ_t (in kPa) for each directly triggered event following Mainshock 14 was 1.03, 0.2, 0.06, and 0.05, respectively (Figure 2.5, Table 2.3). Due to the small size of triggered events (and their associated faults), the orientation and sense of motion along these faults is unknown.

Table 2.3: Transient triggering stresses (τ_t) responsible for directly-triggered earthquakes. Event ID is tied to those of Table 2.1, with event first arrival times in UTC. The τ_t is calculated from the channel component with the highest measured peak ground velocity (PGV$_m$) for station MG02 (Mainshock 5), or station MG05 (Mainshock 14).

Event ID	First arrival	PGV$_m$ (μm/s)	τ_t (kPa)
5	06:22:12	79.06	0.89
14	19:48:01	91.77	1.03
14	19:59:55	18.15	0.20
14	20:25:17	5.30	0.06
14	20:28:07	4.69	0.05

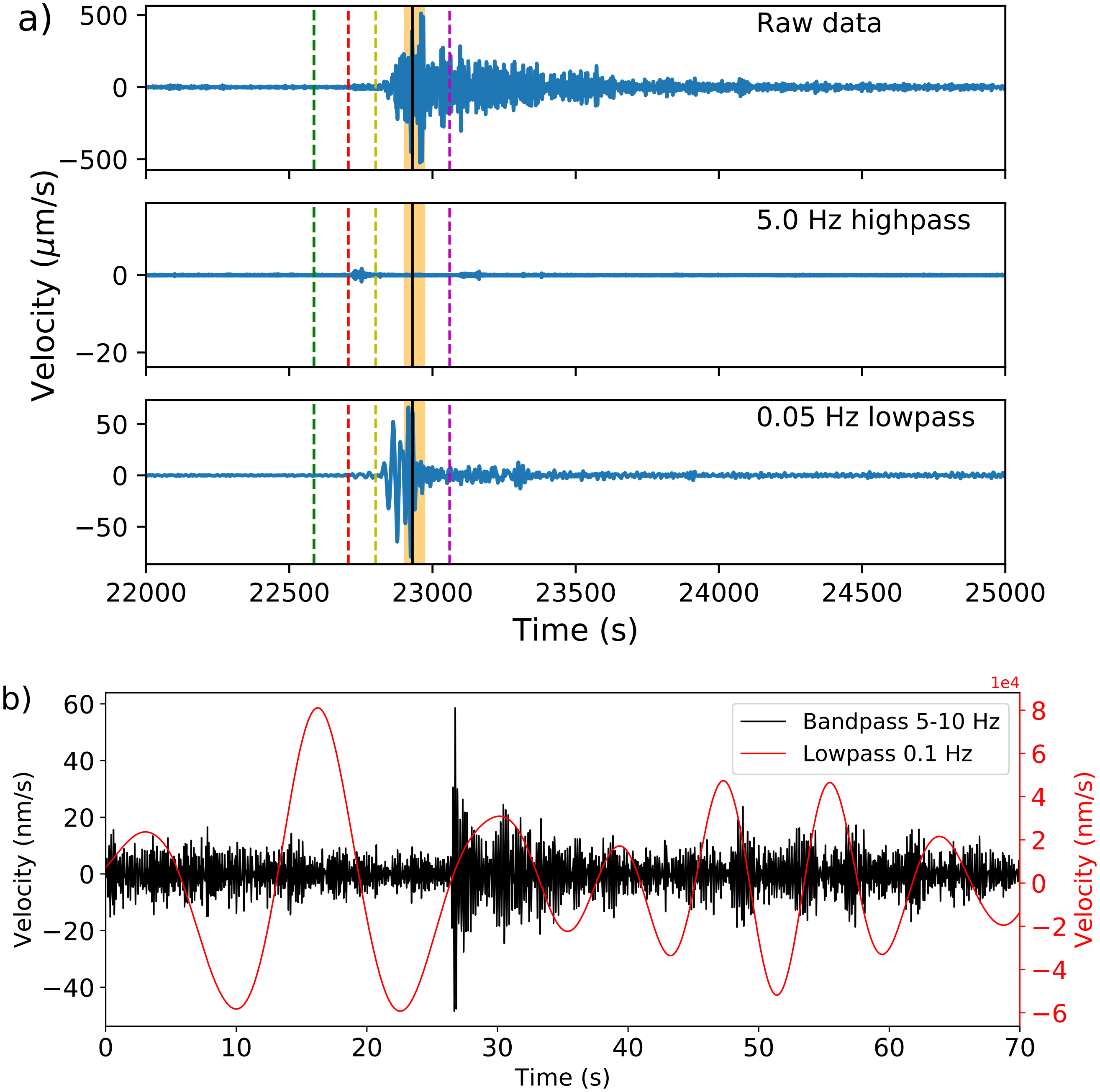

Figure 2.4: a) Vertical seismogram of station MG03 showing velocity for 3 frequency filters over time (in s from start of day) around the 6:16 am (UTC) October 22 2018 mainshock's first arrival (Event 5, Table 2.1). A vertical black line represents the first arrival of the triggered event found during visual analysis. Dashed green and red lines represent the mainshock's origin time and first arrival, while yellow and purple represent surface wave arrivals at 4.4 and 2.0 km/s, respectively. b) View of the triggered event (black) located during visual analysis for the vertical channel. The overlying surface wave energy burying the event is shown in red. The time window is shown in yellow above.

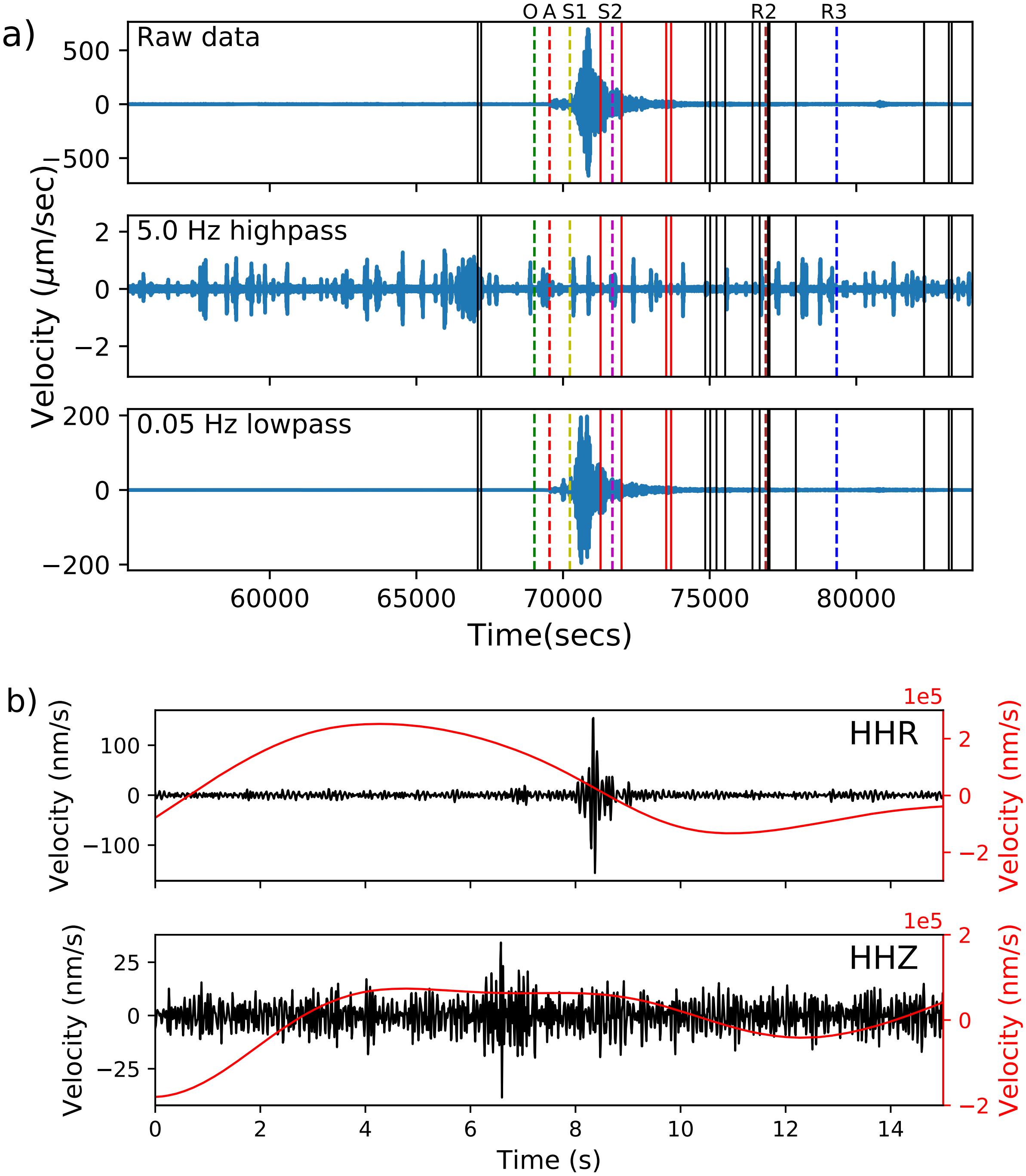

Figure 2.5: a) Vertical seismograms of station MG05 showing velocity alongside 2 frequency filters over time (in s from start of day) for 4 hours before and after the January 28 2020 mainshock's first arrival (Event 14, Table 2.2). The times of earthquakes detected by visual analysis (Table 2.3) are represented by vertical lines, with red for triggered events within the surface wave train, and black for events occurring before the mainshock or after surface wave shaking has reduced close to background levels. Dashed lines represent the mainshock origin time (O, green), first arrival (A, red), surface wave arrivals at 4.4 km/s (S1, yellow) and 2.0 km/s (S2, purple), and the R2 and R3 arrivals as brown and blue lines, respectively, assuming a velocity of 4.4 km/s. b) Seismograms of the radial (HHR) and vertical (HHZ) components for the first triggered event above. The event is visible under an 8-30 Hz bandpass filter (black), with the overlying surface wave energy shown under a 0.1 Hz lowpass filter (red).

Chapter 3

3 Catalogue enhancement using a matched-filter approach

The second approach I take to attempt to indentify dynamic triggering is through the use of a multi-station matched-filter (MMF) method. This method uses all available stations to detect new earthquakes by cross-correlating events from a preexisting earthquake catalogue as templates against continuous waveform data (Chamberlain et al., 2018; Peña Castro et al., 2019; Wang et al., 2019). For this study, I utilize the catalogue published by Roth et al. (2020), with detections automated using a short-term average/long-term average (STA/LTA) technique in the seismological software package $SeisComp3$ (Weber et al., 2007) and, following review by an analyst, had locations calculated by $NonLinLoc$ (Lomax et al., 2000).

The catalogue contained a total of 5945 earthquakes from August 1 2017 to February 2 2020 within the study area (Figure 3.1; Roth et al., 2020). The event magnitudes in this dataset ranged from M_L -0.59 - 4.51, with a magnitude of completeness (M_c) of 1.3, horizontal location errors below 3 km, and epicentral depths of 0.02 - 8.9 km. While this M_c is already quite low, and even comparable to hand-picked catalogues in the KKTA (Visser et al., 2017, 2020), several of the candidate triggering mainshocks had fewer than 10 events in the time range 5 days before and after their arrival (Figure 2.2; Roth et al., 2020). By improving this through catalogue enhancement, I aim to increase the number of detected events, allowing any changes in the seismicity rate following triggering mainshocks to become more apparent. I can then test the reliability of catalogue enhancement by comparing detections to a hand-picked catalogue (Visser et al., 2020) and through visual analysis. The injection data for active wells in the study area is downloaded from the BC Oil and Gas Commission's database (www.bcogc.ca).

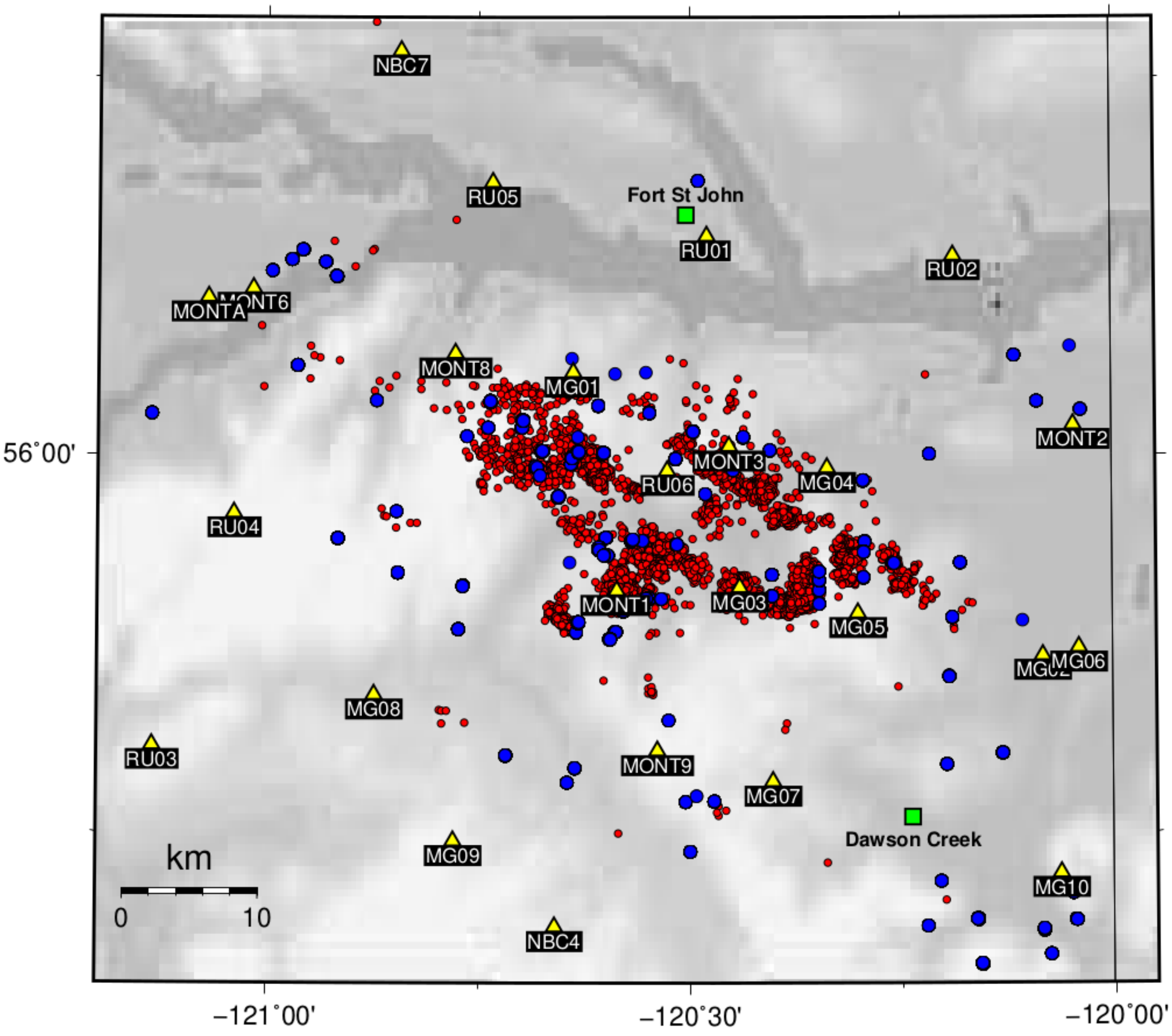

Figure 3.1: Catalogue earthquakes (red circles) in the Kiskatinaw area from August 1 2017 - February 2 2020, including wells with injection activity during this time range (blue circles). Stations are shown as yellow triangles and Dawson Creek and Fort St John are denoted by green squares. The BC-Alberta border is represented as a black line.

3.1 Establishing the multi-station matched-filter

Through $eqcorrscan$, a package in Python that can be used to detect and analyze repeating sequences of earthquakes through the MMF method, I can modify a range of parameters that improve the effectiveness of the MMF, such as the number of templates and frequency range (Chamberlain et al., 2018). The most important of these are the threshold parameter requirements that must be met for a detection to pass my selection criteria, which include the median absolute deviation (MAD) threshold, minimum cross-correlation coefficient (CCC) threshold, frequency range, and the number of phase picks. The MAD threshold only accepts signals with an amplitude of some factor above the background noise level, so a higher level will remove potentially anomalous events or the smallest detected earthquakes. The CCC threshold requires the waveforms from each detection to fit a level of similarity to that of a given template event, so a higher threshold will retain only those events that are the best template matches, resulting in the removal of dissimilar signals. Refining the frequency filter will reduce background noise, resulting in events that are much easier to detect.

To minimize the effects of biases from injection activity and generate sufficient datasets for statistical tests, I enhance the catalogue for a period of 5 days before and after each candidate mainshock. This time range has been shown as an adequate length for observing any increases in seismicity while accounting for injection activity (Wang et al., 2019). Trial tests initially enhanced the catalogue by using up to 12 of the largest catalogue events, centered around the 10 day period, as templates for each candidate triggering mainshock. It was later decided upon to use all of the STA/LTA catalogue events within the 10 day window as template events to achieve the maximum number of potential detections, though this was quite computationally intensive. The detections around each mainshock are then declustered over a range of 5 seconds to remove duplicates.

To determine the optimal set of detection threshold parameters, I set the frequency range to a 3-15 Hz bandpass filter, then compare a variety of MAD and CCC threshold values. I run trial enhancements around Mainshock 14 due to it having the highest number of active stations and a large base of 58 templates (Tables 2.1, A.1; Roth et al., 2020). The MAD threshold is used to separate potential detections from background noise, with previous studies often using a 9x MAD level (Peng and Zhao, 2009; Shelly et al., 2007), so I test trials for 8x MAD and 10x MAD thresholds. Ideally, the higher MAD threshold will result in a lower number of false detections. For the minimum CCC threshold I test a range from 0.4 to 0.6 to potentially allow the MMF to detect events that have dissimilar waveforms from templates. I require at least 4 phase picks for detections to be accepted. This has a dual purpose, as it not only increases the likelihood of detections being real earthquakes (i.e., not local noise detected on a single station), but allows them to potentially be located through the use of $NonLinLoc$ (Lomax et al., 2000). I use the local hybrid velocity model for the KKTA, developed by Roth et al. (2020), featuring a combination of the Crust1.0 (Laske et al., 2013) and Mahani et al. (2017) models. I estimate the magnitude of detected events using the general M_L relation (Richter, 1935):

$$M_L = log(A) - log(A_0), \tag{3.1}$$

in which $log(A)$ is the logarithm of one-half of the peak-to-peak Wood Anderson waveform amplitude (A, in mm), measured from ground motion on the horizontal-component, at a hypocentral distance R (in km), and $-log(A_0)$ is the regional distance correction model evaluated for the same distance R. Peak amplitude is selected within a range of 1s before to 4s after each detection's origin time and, as with the method utilized by Roth et al. (2020), waveforms are filtered over a bandpass of 0.6-40 Hz. This is then adjusted using the local magnitude distance correction model established by Yenier (2017) for the WCSB:

$$-\,logA_0 = 1.399log(R) + 0.001R + 0.102, \tag{3.2}$$

where R is any hypocentral distance < 100 km. My goal during the enhancement process is to achieve the highest number of detections with a false detection rate $< 5\%$.

I use visual analysis for the detections in each trial to confirm that they are real earthquakes. As with the previous visual analysis, for an event to be considered real I must see clear P and S phase arrivals on at least one station. To reduce the time required for visual analysis, I use a python code to compare the origin time of detections for each trial, allowing a time shift of 3 seconds to account for potential errors, and separate out unique events. By doing so I am able to more easily pick out the new events to analyze for each successive trial, rather than look through the entire dataset each time.

3.2 Running the MMF threshold parameter trials

I used a total of 58 catalogue events as templates for the 10 days around Mainshock 14. For the 8x MAD threshold, a minimum 0.5 CCC value resulted in the highest number of detections, but had a false detection rate above 10% and therefore could not be accepted (Figure 3.2). Due to this high false detection rate, it was not necessary to test a lower CCC value at this MAD level. Increasing the CCC threshold to 0.6 dropped the false detection rate to less than 1%, but saw a 35% reduction in the number of detections. The 10x MAD tests had far better results, with the low 0.4 CCC threshold detecting nearly as many events as the 8x MAD 0.5 CCC trial, with just 2 false detections, for a false detection rate of only 0.6% (Figure 3.2). Increasing the CCC threshold to 0.5 resulted in a drop of 36 detections, but also had no evident false detections. The 0.6 CCC trial was not necessary due to the lower level already having a 0% failure rate. While the 8x MAD 0.6 CCC and 10x MAD 0.5 CCC trials are both acceptable due to their low or nonexistent false detection levels, I consider the 10x MAD 0.4 CCC parameters to be the most optimal due to the high number of detections and a false detection rate significantly lower than 5%, despite the low cross-correlation threshold.

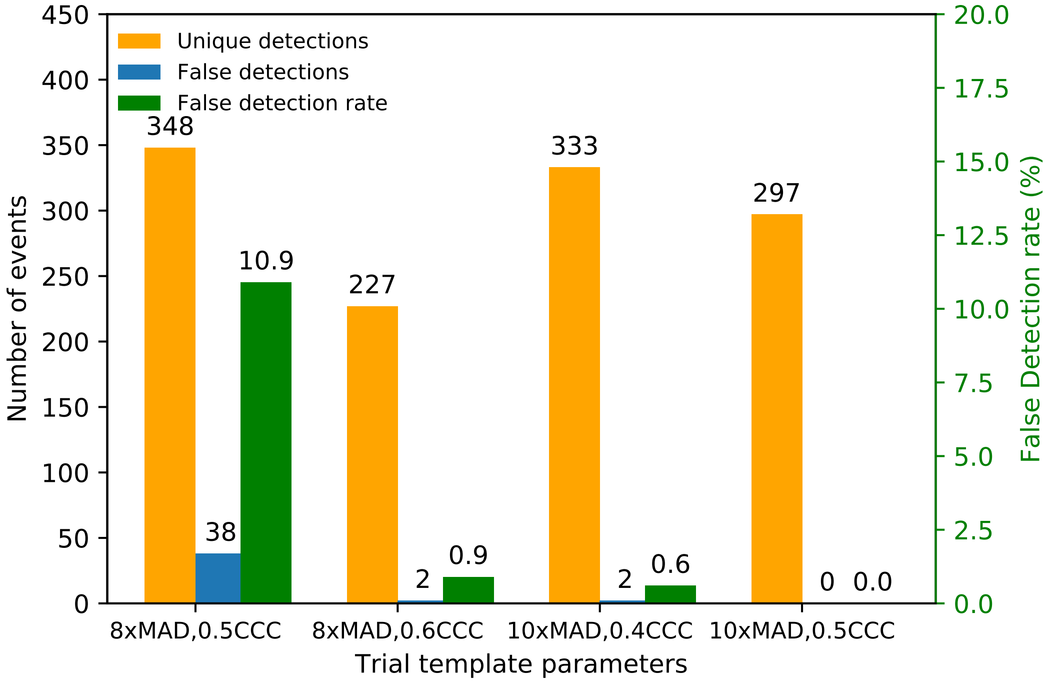

Figure 3.2: Catalogue enhancement results for Mainshock 14 (Table 2.1), for trials testing median absolute deviation and cross-correlation coefficient thresholds over a frequency range of 3-15 Hz. The number of new detections, from a base of 58 templates, are shown in orange, with false detections in blue. The false detection rate (in %) for each trial is shown in green.

Following the tests to locate the optimal threshold parameter pair for MAD and CCC values, I then test an additional set of MMF enhancements to determine the optimal frequency range. I run two new trials of 1-12 Hz and 5-15 Hz bandpass filters for Mainshock 14 in addition to the 3-15 Hz trial from the previous MMF tests. Once again, I perform a visual analysis of detections for the new datasets to locate any false detections or anomalous events.

The MMF enhancement to test various frequency ranges had somewhat unexpected results (Figure 3.3). The lower frequency range of 1-12 Hz had more false detections than the 3-15 Hz range, despite its relatively low number of detections. The 5-15 Hz range, on the other hand, had significantly more unique detections than the lower frequency ranges. Despite having 10 false detections, or 5 times as many as the 3-15 Hz range, the false detection rate was still only 2.5%, and I therefore consider the 5-15 Hz frequency range to be the most optimal.

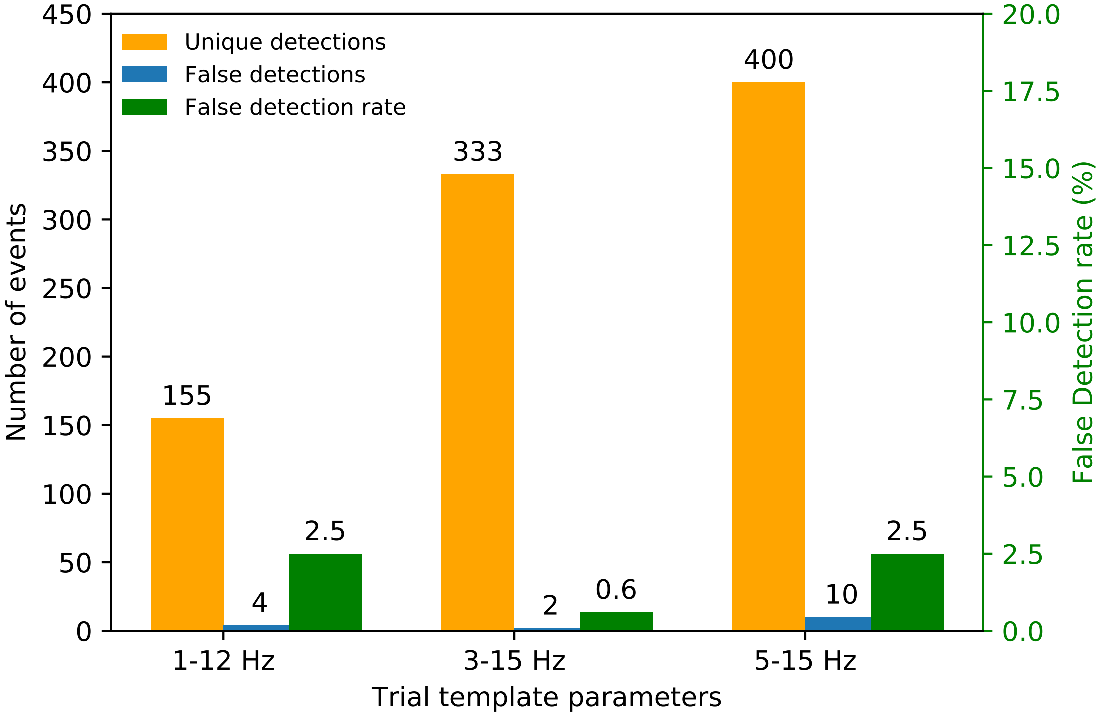

Figure 3.3: Catalogue enhancement results for Mainshock 14 (Table 2.1), for trials testing a variety of frequency ranges. The number of new detections, from a base of 58 templates, are shown in orange, with false detections in blue. The false detection rate for each trial is shown in green (in %). Enhancements are performed using 10x median absolute deviation and 0.4 cross-correlation coefficient thresholds.

To ensure that the optimal MMF enhancement parameters and false detection rate can be applied to the other mainshocks, I use them to enhance detection on September 6 2017, one of the most seismically active days around Mainshock 1. An example of the template matching process is shown in Figure 3.4. As with previous trials, I then visually analyze the detected events to determine the number of false detections. I also compare the results

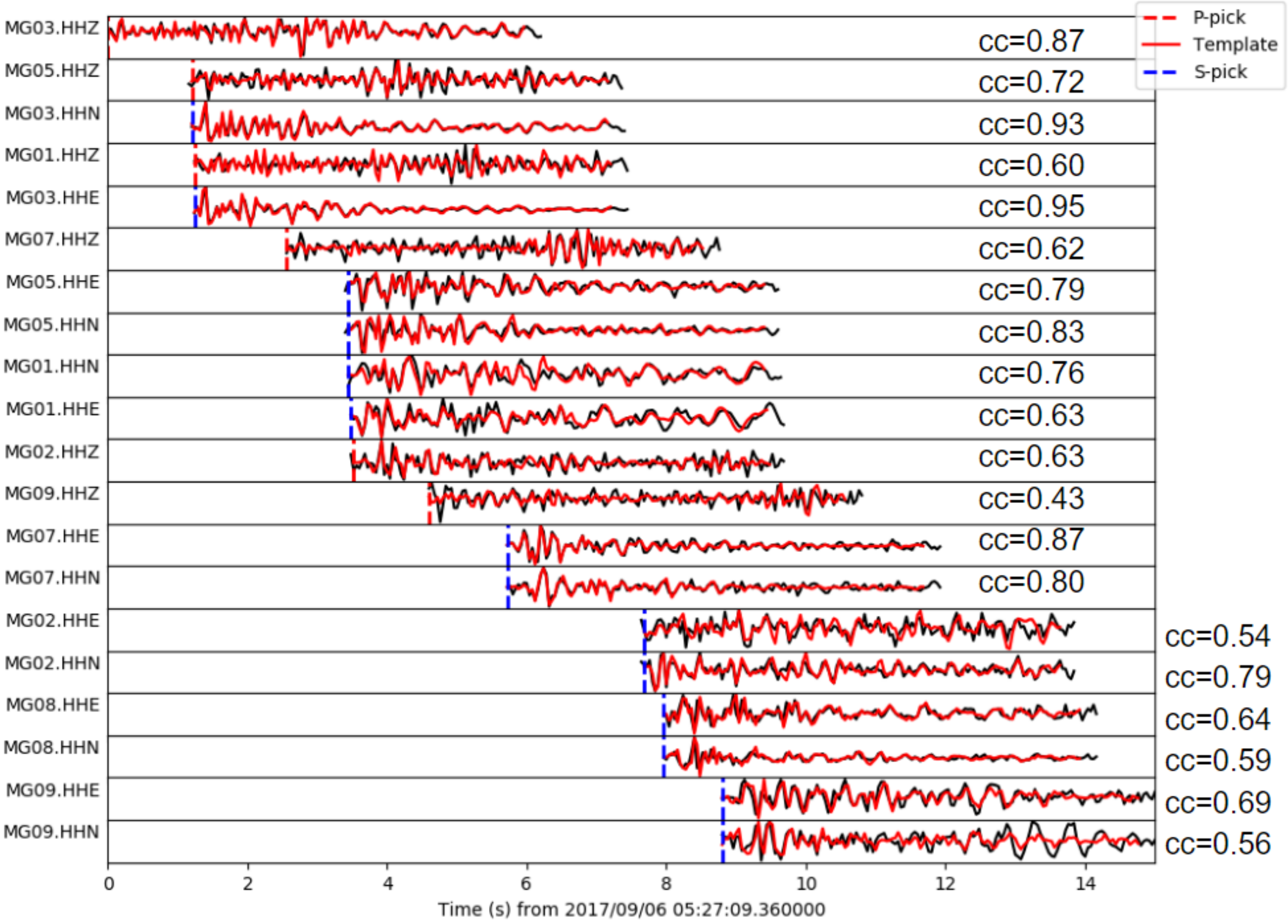

Figure 3.4: An example of the multi-station matched-filter waveform cross correlations for a detection against one of the September 6 2017 templates. Dashed lines show the arrival time of individual phases for each station component, black lines represent the template signal, and red lines are the detection signal. Cross correlation (cc) values are shown on the right.

of the MMF method enhancement against the catalogue in which I had located events by hand for the same time period (Visser et al., 2020). The hand-picked events can be considered a ground truth of real earthquakes, as well as showing the capabilities and quality of an automatically-picked dataset once enhanced. Following this series of tests, I then apply the MMF enhancement to each of the remaining mainshock datasets.

Of the 576 unique detections on September 6 2017, which alone had more detections than the entire 10-day span around Mainshock 14, 22 were not real earthquakes, resulting in a false detection rate of 3.8%. This is still lower than the minimum 5% false detection rate, and I can therefore confirm that these threshold parameters are acceptable. In the comparison against the handpicked catalogue (Visser et al., 2020), the catalogue enhancement only missed 10 earthquakes, but had detected an additional 250 events (after false detections were removed). This implies that enhancing the STA/LTA catalogue was an effective process in capturing earthquakes that are difficult to detect, as the handpicked catalogue was unlikely to miss many earthquakes, save those that did not fit their selection criteria (Visser et al., 2020).

Following catalogue enhancement, the total number of earthquakes between the 8 candidate mainshock datasets varied from as low as just 2 events up to 2123 over the 10-day time intervals (Table 3.1, Figure 3.5). The histograms in Figure 3.6 show the distribution of events for each mainshock over the 10-day spans. To better visualize the relative variation in earthquake numbers, the y axis of each plot was kept constant. The magnitudes of the 3096 detections ranged from M_L -0.87 to 2.4, and while the estimated depths ranged from 0.1-25 km, the events likely occurred at similar depth levels to the catalogue template events (`https://osf.io/qsxhj/`; Roth et al., 2020). Due to it having events concentrated towards the end of the dataset, an additional two days were enhanced for Mainshock 2, which saw a decrease in seismicity outside of the five day mark. Stress contamination likely played a role in the November 30 2018 mainshock dataset, where two local earthquakes with magnitudes $M_W > 4$ occurred within 50 km of the array and may have impacted results (Figure 3.6). The large majority of detections (2743 events) are concentrated around mainshocks 1, 2, and 14. This could be expected, as the 10-day time intervals around each of these mainshocks had the largest number of template events prior to enhancement. Overall, there was approximately an order of magnitude increase in the number of located earthquakes, indicating just how effective the MMF enhancement method was for this region.

Table 3.1: Results following catalogue enhancement for 10 days around each candidate mainshock. Mainshock ID represents the events outlined in Table 2.1. Templates represent the number of original catalogue events, and detections have template events removed. Mainshock events 4 and 5 have been merged due to their identical datasets.

Mainshock ID	Mainshock date	Number of templates	Number of detections
1	2017-09-08	127	1996
2	2018-01-10	94	349
3	2018-01-23	1	118
4,5	2018-10-22	3	3
7	2018-11-30	15	103
8	2018-12-20	7	24
10	2019-07-06	2	0
14	2020-01-28	58	398

The daily volume of injected fluid from wells within 5 km of the templates and event detections, based on the BCOGC well data, is shown in Figure 3.6. There are clear trends in inhibition and enhancement in the seismicity rate following a reduction and increase in the injection volumes, respectively, for candidate mainshocks 1 and 2. They can both be considered to have little to no potential for dynamic triggering to have occurred. The events around Mainshock 3 seem to have a weak correlation, if any, with injection activity, although there is what appears to be a significant increase in seismicity following a delay of one day after the mainshock's arrival. This event in particular really emphasized how critical the catalogue enhancement was for this study, as a single catalogue template event resulted in 118 detections (Table 3.1). Mainshocks 4 and 5 had no active wells within 5 km of detected events, as well as no apparent change in seismicity rate, and too few events to make any meaningful conclusions despite catalogue enhancement. Due to limited injection data, it is difficult to determine a potential correlation with seismicity for Mainshock 7, which also had an apparent inhibition in seismicity despite two large local events preceding the mainshock itself. There was no available injection data within the 10-day period around Mainshock 8, although it does appear to have an increase in seismicity following the teleseismic event. Mainshock 10, like 4 and 5, had far too few events to make conclusions, which could be due to the lack of active wells within 5 km of the events. Mainshock 14 has a clear increase in seismicity, but despite the lack of any available injection data (possibly due to it not being available as of the time of this study), still has a large number of events prior to the mainshock (Figure 3.6). To confirm whether any increases in seismicity following these mainshocks can be considered significant to indicate remote dynamic triggering, I will need to apply a series of statistical tests.

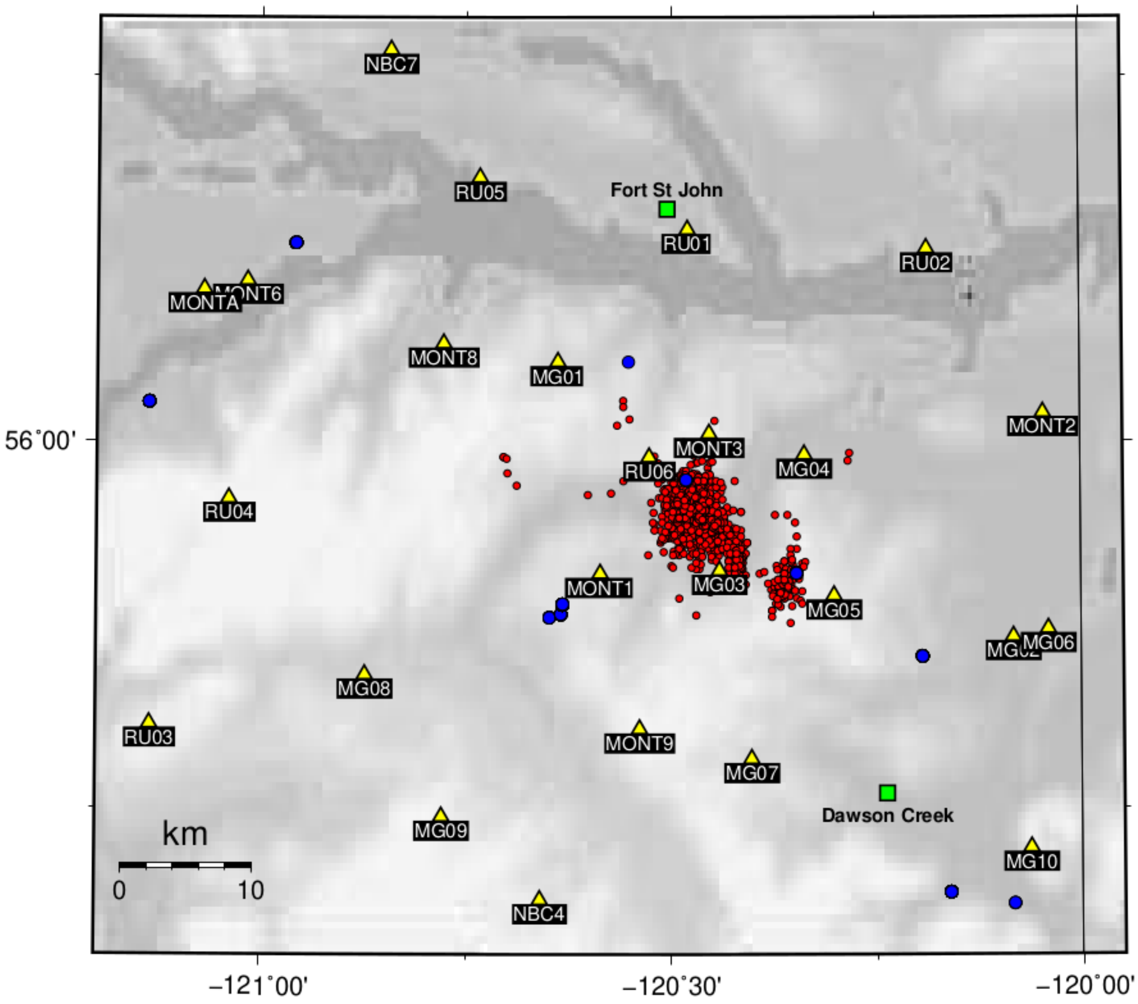

Figure 3.5: Map of detected events (red circles) for Mainshock 1 (Table 2.1) following catalogue enhancement, with active wells during the 10-day time period shown as blue circles. Dawson Creek is denoted by a green square, stations are shown as yellow triangles, and the BC-Alberta border is represented by a black line.

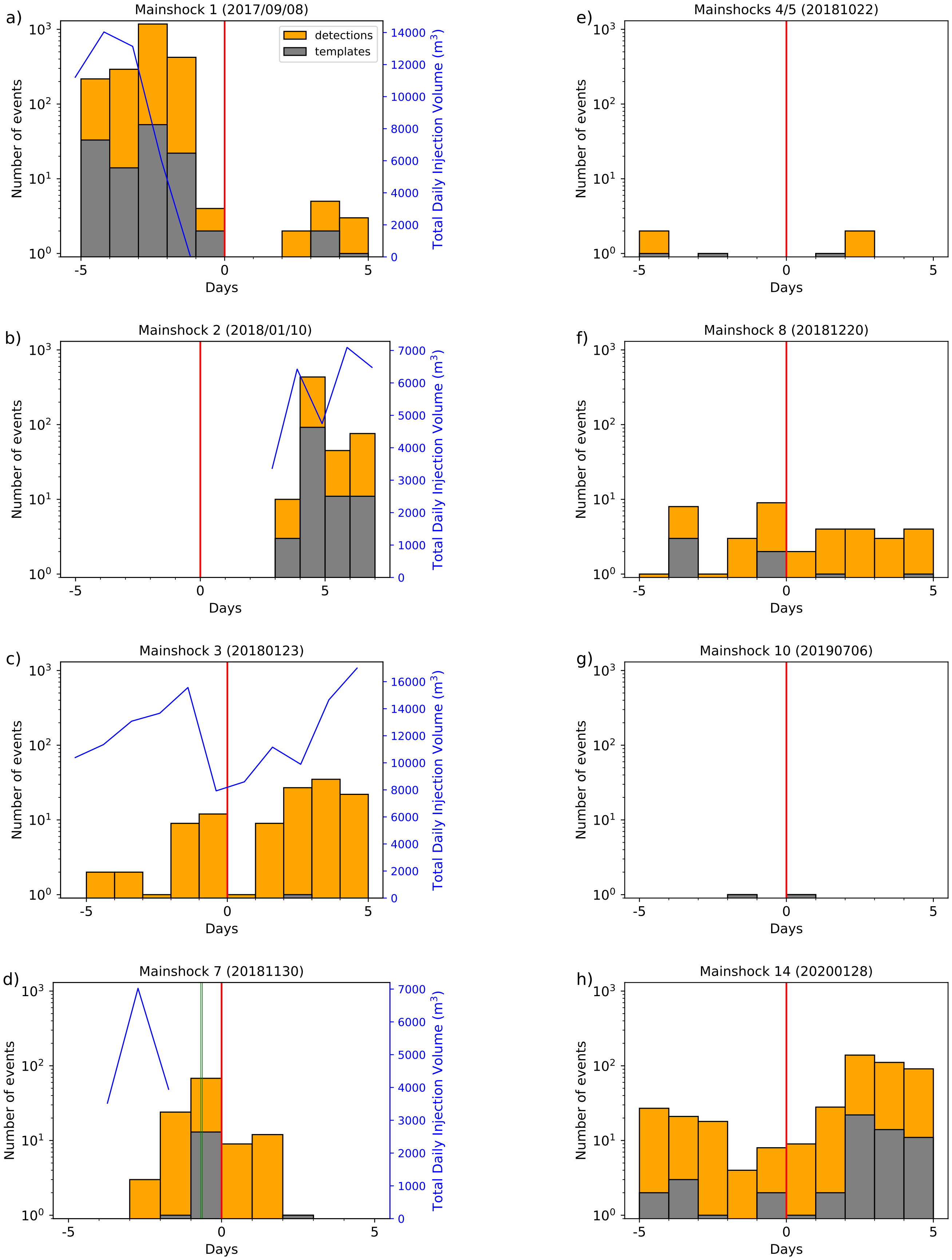

Figure 3.6: Histograms of templates (grey) and detections (orange) resulting from catalogue enhancement for each candidate mainshock. The injection volume from active wells within 5 km of events is represented by blue lines. Red lines denote mainshock first arrivals, and green lines show local mainshock ($M > 4$) origin times.

Chapter 4

4 Statistical tests for dynamic triggering and spectral analysis

4.1 Selection and application of the statistical tests

I apply four statistical tests to each candidate mainshock's dataset to determine if any changes in seismicity following a mainshock's arrival are statistically significant. By doing this series of tests I can accommodate datasets with relatively low levels of seismicity (Marsan and Wyss, 2011; Peña Castro et al., 2019). For each dataset, I denote the number of earthquakes occurring before and after a given mainshock as N_b and N_a, over a time interval of Δt_b and Δt_a, respectively. The rate of earthquakes before and after the potentially triggering mainshocks are denoted by λ_b and λ_a, respectively.

The probability density function (PDF) (Marsan and Wyss, 2011), is shown by:

$$f(\lambda) = \Delta t e^{-\lambda \Delta t} \frac{(\lambda \Delta t)^N}{N!} \tag{4.1}$$

where λ is the seismicity rate for N earthquakes occurring over a time interval Δt. From this, I can combine the PDF's for earthquakes occurring before (N_b at rate λ_b) and after (N_a at rate λ_a) a teleseismic event to calculate the probability of an increase in the seismicity rate increasing more than a predetermined ratio, r. Assuming that the event distribution follows a Poisson process, this can then be represented by:

$$\mathrm{P}\left(\frac{\lambda_a}{\lambda_b}>r\right) = 1 - \frac{1}{N_a!N_b!}\int_0^{\infty} dx\, e^{-x}\, x^{N_b}\, \Gamma(N_a+1, rx) \tag{4.2}$$

where Γ is the incomplete Gamma function (Marsan and Wyss, 2011).

In this case, P represents the probability that the rate of earthquakes after an event will be r times greater than the rate of earthquakes before it. The probability $P = \mathrm{P}(\frac{\lambda_a}{\lambda_b} > 1)$ can be used to compare the difference between the rate of earthquakes before and after the event. Therefore, a P value of 0.5 represents no change in the rate of seismicity, while a value approaching 1 or 0 represent an increase or decrease in seismicity, respectively. For example, for P = 0.995, there is only a 0.5% probability that there has been no increase in the seismicity rate. A secondary statistic, γ, is used to represent the log of the separation from P = 0.5, so for P values $<$ 0.5:

$$\gamma = log_{10}\, P \tag{4.3}$$

can be used, and for $P >$ 0.5,

$$\gamma = -\, log_{10}(1 - P) \tag{4.4}$$

is used instead (Marsan and Nalbant, 2005). A confidence level of 95% for significant increases in seismicity would therefore require $P \geq$ 0.975 and $\gamma \geq$ 1.6 (Marsan and Wyss, 2011).

The β statistic (Matthews and Reasenberg, 1988) is commonly used for investigating seismicity rate changes, and measures the number of events that occurred against those that would be expected over a given time window (Gomberg et al., 2001; Hill and Prejean, 2015; Husker and Brodsky, 2004; Johnson and Bürgmann, 2016). This is then scaled by the standard deviation to get:

$$\beta = \frac{N_a - (N_b \times \frac{\Delta t_a}{\Delta t_b})}{\sqrt{(N_b \times \frac{\Delta t_a}{\Delta t_b})}}. \tag{4.5}$$

The main weakness of the β statistic is due to it only being normalized by the number of events before each mainshock, so is heavily impacted by low N_b numbers. To get around this, I also utilize the Z statistic (Habermann, 1981), which is a symmetric version of the β statistic and is less dependant on N_b:

$$Z = \frac{N_a\,\Delta t_b - N_b\,\Delta t_a}{\sqrt{N_a\,\Delta t_b^2 + N_b\,\Delta t_a^2}}. \tag{4.6}$$

For a 95% confidence interval I would require β and Z statistic values ≥ 2.

The codes for each statistical test are written into MATLAB, which has predesignated functions for calculating the probability of a seismicity rate increase as well as the β statistic (MATLAB, 2018). For an increase in seismicity to be considered statistically significant, I require the results for each mainshock to pass all four thresholds of: $P \geq 0.975$, $\gamma \geq 1.6$, $\beta \geq 2.0$, and $Z \geq 2.0$. These thresholds have been used to define statistical significance in previous work at the 95% confidence level (Aiken and Peng, 2014; Marsan and Wyss, 2011; Peña Castro et al., 2019; Wang et al., 2019).

4.2 Statistical test results

With mainshocks 4 and 5 being merged due to their close temporal proximity and having identical detections, I was left with 8 enhanced catalogue datasets to run the statistical tests on. As shown in Table 4.1, Mainshocks 2, 3, and 14 satisfy the criteria of passing each of the statistical thresholds, and can be considered to exhibit significant increases in seismicity. Mainshock 8 saw an increase in seismicity as well, although that event's dataset only passed the β statistic threshold (Table 4.1). The remaining four candidate mainshocks saw a reduction or no change in seismicity.

Table 4.1: Statistical test results for each of the candidate mainshock enhanced datasets. Event ID represents the mainshocks as outlined by Table (2.1). Nb and Na represent the number of events before and after a given mainshock's arrival time, respectively. Events that pass all four statistical thresholds are shown in bold.

Event ID	Nb	Na	P	γ	β	Z	Rate Change
1	2200	10	8.11e-07	-6.09	-45.75	-45.64	Decrease
2	0	443	1	Infinity	Infinity	21.04	**Increase**
3	26	93	1	11.27	13.14	6.14	**Increase**
4,5	3	3	0.5	0.3	0	0	No Change
7	116	22	7.37e-06	-5.13	-8.73	-8.0	Decrease
8	11	20	0.95	1.26	2.71	1.62	Increase
10	1	1	0	0	0.5	0.3	No Change
14	79	377	1	Infinity	33.53	13.96	**Increase**

Out of the 9 candidate triggering mainshocks, 5 indicate the potential occurrence of dynamic triggering between the visual analysis and catalogue enhancement methods. Despite a statistically-significant increase in seismicity, Mainshock 2 can not be accepted as a case of dynamic triggering due to the lack of any catalogue events or detections until four days after the mainshock's arrival, and its clear association of seismicity with injection activity (Figure 3.6). While the seismicity increase after Mainshock 8 only passed one statistical significance threshold (Table 4.1), it may still be a case of dynamic triggering due to the lack of any injection activity and doubling of seismicity following the passage of transient stresses. Mainshock 5 resulted in a directly triggered earthquake detected during visual analysis, but did not show an increase in seismicity following enhancement and statistical tests. Mainshocks 4 and 10 similarly saw no changes in seismicity, and had very small numbers of earthquakes. This may have been a side effect of the lack of injection wells located within 5 km of its events, leading to relatively low induced seismicity prior to the mainshock. Mainshock 3 showed strong statistical evidence of remote dynamic triggering, as well as a potential correlation of seismicity with injection (Table 4.1, Figure 3.6). Mainshock 14, located near Cuba, was not only the most distant candidate mainshock, but was the only event to show strong evidence of triggered seismicity in both the visual analysis and statistical tests, as well as lacking any apparent injection activity (Figure 3.6).

The three mainshocks with clear indications of dynamic triggering (3, 5, and 14), had epicentral depths within 16.2-33.6 km and three of the four highest τ measurements at 13.75, 5.02, and 7.05 kPa, respectively (Tables 2.1, 2.2). Mainshock 8, if accepted, would similarly have a depth of 17.1 km, but with a lower τ of 2.73 kPa. Mainshock 1 was one of the deepest of the candidate mainshocks at 44.8 km, and despite having the highest τ at 16.13 kPa, did not trigger seismicity. These results suggest that there may be something else involved that causes only some of the mainshocks to result in dynamic triggering.

Chapter 5

Discussion and Conclusions

5.1 Comparison of results with other studies

There appears to be no clear correlation between each mainshock's focal mechanism, PGV$_m$, and magnitude on the occurrence of dynamic triggering. It is evident that the candidate mainshock with the highest magnitude and associated PGV$_m$ (M$_S$ 8.2, Event 1) did not trigger seismicity, while the event with the second lowest magnitude (M$_S$ 8.2 Event 5) resulted in a directly triggered earthquake. While two of the three candidate mainshocks with clear evidence of triggering are strike-slip events (Events 5,14), and the third slipped along a thrust fault (Event 3), this does not indicate a correlation among the 9 focal mechanisms available (Figure 2.3). There is, however, a clear indication of transient stresses roughly equivalent to tidal stresses ($\sim$10 kPa, Cochran et al., 2004) being responsible for triggering seismicity, with observed τ of triggering mainshocks spanning approximately 5 - 16 kPa (Table 2.2). The observed τ_t capable of directly triggering seismicity fell within 0.05 - 1.03 kPa (Figure 2.3), which was lower than the previously observed dynamic triggering thresholds found in the WCSB of 0.16 kPa (Wang et al., 2015) and 1.7 kPa (Wang et al., 2019). These low triggering stresses imply that many of the unmapped faults in the KKTA are critically stressed, due to the increased fluid pressures along faults nearby injection wells. The detection of these triggered events would not have been possible without the recent seismic network additions featured in this study. It is probable that the minimum threshold for dynamic triggering may be lower even than the levels found here, and a recent study showed that mining activity in northeastern BC triggered earthquakes with peak dynamic strain as low as 1.0×10^{-9} (Dokht et al., 2020).

Based on the BCOGC well data, there was no published injection activity for Mainshocks 8 and 14, suggesting that the seismicity for those datasets may have been encouraged by high residual pore fluid pressures, which can be retained at levels high enough to promote earthquake nucleation for months following injection activity (Atkinson et al., 2016; Farahbod et al., 2015; Flewelling and Sharma, 2014). The events that appear to correlate with changes in the injection rate seem to result in alterations in the seismicity rate within 2 days (Figure 3.6).

5.2 Spectral analysis

The triggered events detected in this study occurred anywhere from seconds after the arrival of teleseismic waves to several hours, or even days, after their passage. This has been shown in previous studies where triggered events were found buried within the surface wave train (Hill et al., 1993; Husker and Brodsky, 2004; Velasco et al., 2008; Wang et al., 2019, 2015), delayed by hours (Johnson and Bürgmann, 2016; Peña Castro et al., 2019), or observed as a seismicity rate increase over a scale of days (Gomberg et al., 2001; Wang et al., 2019). Possible mechanisms for delayed triggering include: surface waves causing aseismic creep (Shelly et al., 2011), dynamic stresses unclogging fractures, leading to an increase in permeability and therefore pore fluid pressures (Elkhoury et al., 2006; Manga et al., 2012), or — on a scale of minutes — the rate-state frictional failure could be responsible, in which transient stresses alter the friction on a fault, promoting slip (Brodsky and van der Elst, 2014; Gomberg et al., 2001). Low frequency shaking from surface waves can also magnify the stresses of fluid-filled fractures by over 2 orders of magnitude, which could enhance the possibility of the fracture unclogging process to result in triggered events (Zheng, 2018). It is plausible that a number of these mechanisms could be at least partially responsible for the observed delayed triggering.

To determine if long period shaking is at least partially responsible for dynamic triggering, I plot the vertical ground velocity spectra of each mainshock for station MG09 of the XL network. This station was selected due to having the most sensitive high broadband instrument, and is therefore adequate for visualizing low frequency data down to 0.009 Hz following instrument response removal. To do this I use the Python wrapper mtspec to apply a multitaper fourier transform to the waveform data, with 7 tapers and a time bandwidth of 3.5 s (Prieto et al., 2009). To focus on the surface wave energy, I trim the data for a time interval measured to 5 s before and 1795 s after the approximate surface wave arrivals, which were determined visually, for a total span of 30 minutes (Figure 5.1).

The results of the spectral analysis also appear to show no clear pattern between the candidate mainshocks that did or did not trigger seismicity (Figure 5.2). While two events with clear evidence of dynamic triggering, Mainshocks 3 and 14, have the highest amplitudes around lower frequencies of 0.07 - 0.1 Hz, Mainshock 1 had the strongest energy below those frequencies, despite the changes in its seismicity rate appearing to solely correlate with injection activity (Figure 3.6). Mainshocks 5 and 8 had relatively low amplitudes at the lower frequencies, although the former became nearly the highest from frequencies of 0.1 - 0.8 Hz (Figure 5.2).

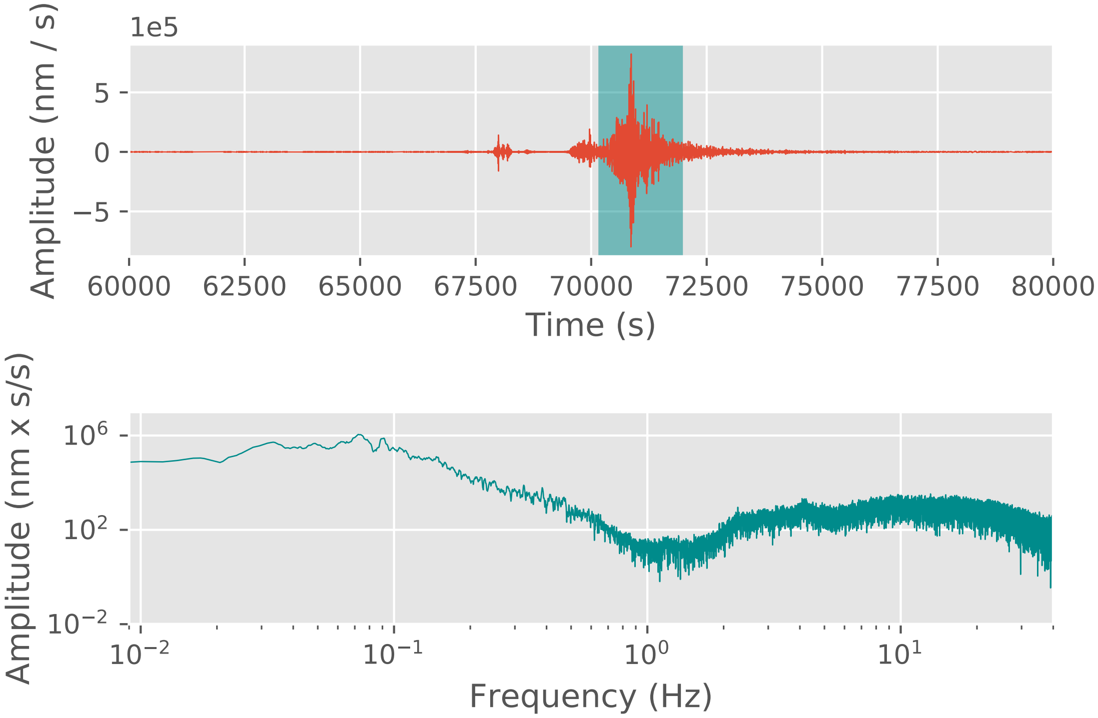

Figure 5.1: Top: Vertical seismogram of station MG09 for Mainshock 14 (Table 2.1), with time in seconds from start of day. The time interval for the spectral analysis is outlined by the green bar. Bottom: Vertical ground velocity spectra for the time interval shown above.

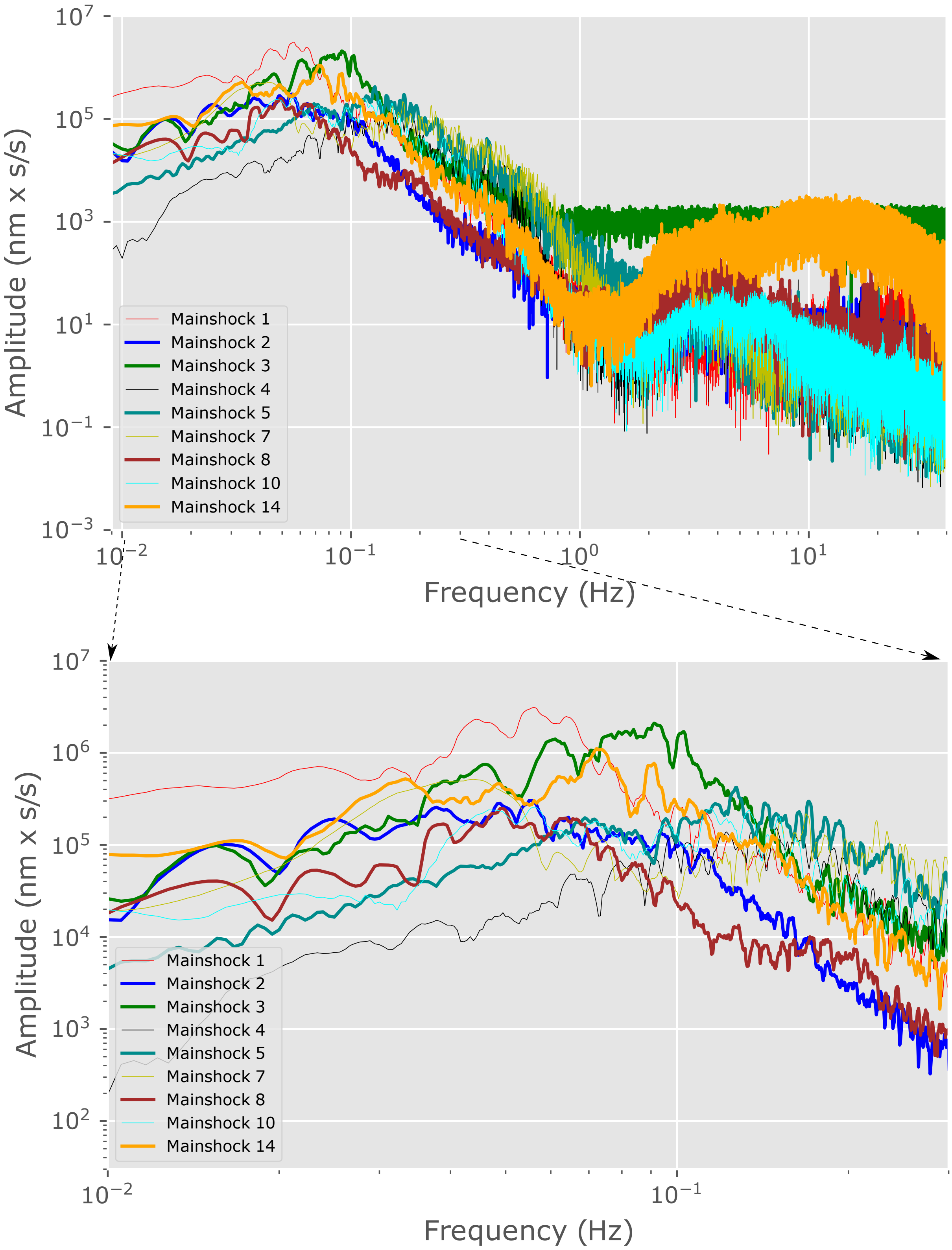

Figure 5.2: Vertical ground velocity spectra for all potentially triggering mainshocks, with events showing evidence of dynamic triggering shown in bold. (Top) Spectra shown over the frequency range of 0.009 - 40 Hz. (Bottom) Spectra shown over a more focused frequency range of 0.01 - 0.3 Hz.

5.3 Conclusions and future work

In this study, I find strong evidence of remote dynamic triggering in the KKTA through visual analysis and the use of MMF catalogue enhancement methods. I visually detect triggered earthquakes in two of nine candidate mainshocks occurring within the surface wave train to nearly four hours after their passage. Following catalogue enhancement, I perform the P, γ, β, and Z statistical tests to confirm that any increases in seismicity rate following each mainshock's arrival are significant enough to indicate triggering. I determine that two mainshocks have significant increases in seismicity, as well as potential triggering from a third event that did not pass all four statistical tests (Table 4.1). A total of 4 unique candidate mainshocks indicate the potential for remote dynamic triggering, with τ of triggering mainshocks from 2.73 - 16.13 kPa (Table 2.2), and observed τ_t responsible for directly triggering seismicity as low as 0.05 kPa (Table 2.3). Two of these mainshocks had no apparent injection activity during the enhancement period, and epicentral depths of triggering events ranged from 10 - 17 km (Table 2.1).

I show the improvement in seismicity detection rates due to the new, dense local seismic network. The MMF method was very effective in enhancing the baseline STA/LTA catalogue for 10 days around most of the candidate mainshock datasets. The best example of this was for Event 3, in which a single template earthquake detected 118 events, and outlined a significant increase in seismicity following the mainshock's arrival (Table 3.1). It is possible that some of the increases in seismicity found in this study resulted solely due to injection activity, such as the increase following Event 2 in Figure 3.6, rather than the influence of transient stresses from large, distant events, or from a combination of injection and transient stresses. This combination of active injection and incoming surface waves likely played a role in the seismicity increase observed following Event 3 (Figure 3.6). The MMF threshold parameters I use in this study, with a 10x MAD, 0.4 CCC, 3-15 Hz frequency range, and minimum of 4 phase picks, are very efficient in maximizing the number of detections while retaining false detection rates well below 5% (Figures 3.2, 3.3). The time lag between the arrival of teleseismic surface waves and triggered seismicity varied from a scale of seconds to several days (Figure 3.6). Further seismicity studies in this region are much more feasible due to station density in the KKTA continuing to increase over time.

Glossary

BCOGC The BC Oil and Gas Commission.

CCC Cross correlation coefficient, attained by directly comparing the similarity of two waveforms over a given time window, with higher values indicating stronger similarity, normalized from 0 to 1.

KKTA Kiskatinaw area, also referred to as the Kiskatinaw Seismic Monitoring and Mitigation Area by the BC Oil and Gas Commission, located around Dawson Creek, British Columbia.

MAD Median absolute deviation, a measure of the strength or amplitude of a seismic signal, where a higher MAD value can be used to separate a signal from anomalous background noise.

PGV$_m$ Measured peak ground velocity.

PGV$_R$ Measured peak ground velocity on the radial station component (orientated towards incoming waves).

PGV$_T$ Measured peak ground velocity on the transverse station component (orientated perpendicular to incoming waves).

PGV$_t$ Theoretical peak ground velocity.

PGV$_Z$ Measured peak ground velocity on the vertical station component.

Bibliography

Aiken, C. and Peng, Z. (2014). Dynamic triggering of microearthquakes in three geothermal/volcanic regions of california. *Journal of Geophysical Research: Solid Earth*, 119(9):6992–7009.

Aki, K. and Richards, P. G. (2002). Quantitative seismology, sausalito.

Atkinson, G. M., Eaton, D. W., Ghofrani, H., Walker, D., Cheadle, B., Schultz, R., Shcherbakov, R., Tiampo, K., Gu, J., Harrington, R. M., et al. (2016). Hydraulic fracturing and seismicity in the western canada sedimentary basin. *Seismological Research Letters*, 87(3):631–647.

Beeler, N. and Lockner, D. (2003). Why earthquakes correlate weakly with the solid earth tides: Effects of periodic stress on the rate and probability of earthquake occurrence. *Journal of Geophysical Research: Solid Earth*, 108(B8).

Brodsky, E. E., Karakostas, V., and Kanamori, H. (2000). A new observation of dynamically triggered regional seismicity: Earthquakes in greece following the august 1999 izmit, turkey earthquake. *Geophysical Research Letters*, 27(17):2741–2744.

Brodsky, E. E. and Prejean, S. G. (2005). New constraints on mechanisms of remotely triggered seismicity at long valley caldera. *Journal of Geophysical Research: Solid Earth*, 110(B4).

Brodsky, E. E. and van der Elst, N. J. (2014). The uses of dynamic earthquake triggering.

Chamberlain, C. J., Hopp, C. J., Boese, C. M., Warren-Smith, E., Chambers, D., Chu, S. X., Michailos, K., and Townend, J. (2018). Eqcorrscan: Repeating and near-repeating earthquake detection and analysis in python. *Seismological Research Letters*, 89(1):173–181.

Cochran, E. S., Vidale, J. E., and Tanaka, S. (2004). Earth tides can trigger shallow thrust fault earthquakes. *Science*, 306(5699):1164–1166.

Crotwell, H. P., Owens, T. J., and Ritsema, J. (1999). The taup toolkit: Flexible seismic travel-time and ray-path utilities. *Seismological Research Letters*, 70(2):154–160.

Dokht, R. M., Smith, B., Kao, H., Visser, R., and Hutchinson, J. (2020). Reactivation of an intraplate fault by mine-blasting events: Implications to regional seismic hazard in western canada. *Journal of Geophysical Research: Solid Earth*, page e2020JB019933.

Dziewonski, A., Chou, T.-A., and Woodhouse, J. H. (1981). Determination of earthquake source parameters from waveform data for studies of global and regional seismicity. *Journal of Geophysical Research: Solid Earth*, 86(B4):2825–2852.

Dziewonski, A. M. and Anderson, D. L. (1981). Preliminary reference earth model. *Physics of the earth and planetary interiors*, 25(4):297–356.

Ekström, G., Nettles, M., and Dziewoński, A. (2012). The global cmt project 2004–2010: Centroid-moment tensors for 13,017 earthquakes. *Physics of the Earth and Planetary Interiors*, 200:1–9.

Elkhoury, J. E., Brodsky, E. E., and Agnew, D. C. (2006). Seismic waves increase permeability. *Nature*, 441(7097):1135–1138.

Ellsworth, W. L. (2013). Injection-induced earthquakes. *Science*, 341(6142).

Farahbod, A. M., Kao, H., Cassidy, J. F., and Walker, D. (2015). How did hydraulic-fracturing operations in the horn river basin change seismicity patterns in northeastern british columbia, canada? *The Leading Edge*, 34(6):658–663.

Flewelling, S. A. and Sharma, M. (2014). Constraints on upward migration of hydraulic fracturing fluid and brine. *Groundwater*, 52(1):9–19.

Gomberg, J., Reasenberg, P., Bodin, P. l., and Harris, R. (2001). Earthquake triggering by seismic waves following the landers and hector mine earthquakes. *Nature*, 411(6836):462–466.

Grigoli, F., Cesca, S., Priolo, E., Rinaldi, A. P., Clinton, J. F., Stabile, T. A., Dost, B., Fernandez, M. G., Wiemer, S., and Dahm, T. (2017). Current challenges in monitoring, discrimination, and management of induced seismicity related to underground industrial activities: A european perspective. *Reviews of Geophysics*, 55(2):310–340.

Habermann, R. (1981). Precursory seismicity patterns: stalking the mature seismic gap. *Earthquake prediction: An international review*, 4:29–42.

Healy, J., Hamilton, R., and Raleigh, C. (1970). Earthquakes induced by fluid injection and explosion. *Tectonophysics*, 9(2-3):205–214.

Hill, D. P. and Prejean, S. (2015). Dynamic triggering.

Hill, D. P., Reasenberg, P., Michael, A., Arabaz, W., Beroza, G., Brumbaugh, D., Brune, J., Castro, R., Davis, S., dePolo, D., et al. (1993). Seismicity remotely triggered by the magnitude 7.3 landers, california, earthquake. *Science*, 260(5114):1617–1623.

Hough, S. E. and Kanamori, H. (2002). Source properties of earthquakes near the salton sea triggered by the 16 october 1999 m 7.1 hector mine, california, earthquake. *Bulletin of the Seismological Society of America*, 92(4):1281–1289.

Husker, A. L. and Brodsky, E. E. (2004). Seismicity in idaho and montana triggered by the denali fault earthquake: A window into the geologic context for seismic triggering. *Bulletin of the Seismological Society of America*, 94(6B):S310–S316.

Johnson, C. W. and Bürgmann, R. (2016). Delayed dynamic triggering: Local seismicity leading up to three remote m 6 aftershocks of the 11 april 2012 m8. 6 indian ocean earthquake. *Journal of Geophysical Research: Solid Earth*, 121(1):134–151.

Kao, H., Hyndman, R., Jiang, Y., Visser, R., Smith, B., Babaie Mahani, A., Leonard, L., Ghofrani, H., and He, J. (2018a). Induced seismicity in western canada linked to tectonic strain rate: Implications for regional seismic hazard. *Geophysical Research Letters*, 45(20):11–104.

Kao, H., Visser, R., Smith, B., and Venables, S. (2018b). Performance assessment of the induced seismicity traffic light protocol for northeastern british columbia and western alberta. *The Leading Edge*, 37(2):117–126.

Laske, G., Masters, G., Ma, Z., and Pasyanos, M. (2013). Update on crust1. 0—a 1-degree global model of earth's crust. In *Geophysical Research Abstracts*, volume 15, page 2658.

Lay, T. and Wallace, T. C. (1995). *Modern global seismology*. Elsevier.

Lomax, A., Virieux, J., Volant, P., and Berge-Thierry, C. (2000). Probabilistic earthquake location in 3d and layered models. In *Advances in seismic event location*, pages 101–134. Springer.

Love, A. E. H. (1927). *A treatise on the mathematical theory of elasticity*. Cambridge University Press.

Mahani, A. B., Schultz, R., Kao, H., Walker, D., Johnson, J., and Salas, C. (2017). Fluid injection and seismic activity in the northern montney play, british columbia, canada, with special reference to the 17 august 2015 m w 4.6 induced earthquake. *Bulletin of the Seismological Society of America*, 107(2):542–552.

Manga, M., Beresnev, I., Brodsky, E. E., Elkhoury, J. E., Elsworth, D., Ingebritsen, S. E., Mays, D. C., and Wang, C.-Y. (2012). Changes in permeability caused by transient stresses: Field observations, experiments, and mechanisms. *Reviews of Geophysics*, 50(2).

Marsan, D. and Nalbant, S. S. (2005). Methods for measuring seismicity rate changes: A review and a study of how the m w 7.3 landers earthquake affected the aftershock sequence of the m w 6.1 joshua tree earthquake. *Pure and Applied Geophysics*, 162(6-7):1151–1185.

Marsan, D. and Wyss, M. (2011). Seismicity rate changes. *Community Online Resource for Statistical Seismicity Analysis*.

MATLAB (2018). *9.7.0.1190202 (R2019b)*. The MathWorks Inc., Natick, Massachusetts.

Matthews, M. V. and Reasenberg, P. A. (1988). Statistical methods for investigating quiescence and other temporal seismicity patterns. *Pure and Applied Geophysics*, 126(2-4):357–372.

McGarr, A., Simpson, D., Seeber, L., and Lee, W. (2002). Case histories of induced and triggered seismicity. *International Geophysics Series*, 81(A):647–664.

Pearson, C. (1981). The relationship between microseismicity and high pore pressures during hydraulic stimulation experiments in low permeability granitic rocks. *Journal of Geophysical Research: Solid Earth*, 86(B9):7855–7864.

Peña Castro, A., Dougherty, S. L., Harrington, R., and Cochran, E. S. (2019). Delayed dynamic triggering of disposal-induced earthquakes observed by a dense array in northern oklahoma. *Journal of Geophysical Research: Solid Earth*, 124(4):3766–3781.

Peng, Z. and Zhao, P. (2009). Migration of early aftershocks following the 2004 parkfield earthquake. *Nature Geoscience*, 2(12):877–881.

Prejean, S., Hill, D., Brodsky, E., Hough, S., Johnston, M., Malone, S., Oppenheimer, D., Pitt, A., and Richards-Dinger, K. (2004). Remotely triggered seismicity on the united states west coast following the mw 7.9 denali fault earthquake. *Bulletin of the Seismological Society of America*, 94(6B):S348–S359.

Prieto, G., Parker, R., and Vernon III, F. (2009). A fortran 90 library for multitaper spectrum analysis. *Computers & Geosciences*, 35(8):1701–1710.

Pyrocko (2018). *Pyrocko: A Versatile Seismology Toolkit for Python*. Version 2018.1.29, http://pyrocko.org.

Richter, C. F. (1935). An instrumental earthquake magnitude scale. *Bulletin of the seismological society of America*, 25(1):1–32.

Roth, M. P., Verdecchia, A., Harrington, R. M., and Liu, Y. (2020). High-resolution imaging of hydraulic-fracturing-induced earthquake clusters in the dawson-septimus area, northeast british columbia, canada. *Seismological Research Letters*.

Schultz, R., Atkinson, G., Eaton, D., Gu, Y., and Kao, H. (2018). Hydraulic fracturing volume is associated with induced earthquake productivity in the duvernay play. *Science*, 359(6373):304–308.

Schultz, R., Stern, V., Gu, Y. J., and Eaton, D. (2015). Detection threshold and location resolution of the alberta geological survey earthquake catalogue. *Seismological Research Letters*, 86(2A):385–397.

Shelly, D. R., Beroza, G. C., and Ide, S. (2007). Non-volcanic tremor and low-frequency earthquake swarms. *Nature*, 446(7133):305–307.

Shelly, D. R., Peng, Z., Hill, D. P., and Aiken, C. (2011). Triggered creep as a possible mechanism for delayed dynamic triggering of tremor and earthquakes. *Nature Geoscience*, 4(6):384–388.

Telford, W. M., Telford, W., Geldart, L., Sheriff, R. E., and Sheriff, R. (1990). *Applied geophysics*. Cambridge university press.

van der Elst, N. J. and Brodsky, E. E. (2010). Connecting near-field and far-field earthquake triggering to dynamic strain. *Journal of Geophysical Research: Solid Earth*, 115(B7).

van der Elst, N. J., Savage, H. M., Keranen, K. M., and Abers, G. A. (2013). Enhanced remote earthquake triggering at fluid-injection sites in the midwestern united states. *Science*, 341(6142):164–167.

Velasco, A. A., Ammon, C. J., Farrell, J., and Pankow, K. (2004). Rupture directivity of the 3 november 2002 denali fault earthquake determined from surface waves. *Bulletin of the Seismological Society of America*, 94(6B):S293–S299.

Velasco, A. A., Hernandez, S., Parsons, T., and Pankow, K. (2008). Global ubiquity of dynamic earthquake triggering. *Nature Geoscience*, 1(6):375–379.

Vincenty, T. (1975). Direct and inverse solutions of geodesics on the ellipsoid with application of nested equations. *Survey Review*, 23(176):88–93.

Visser, R., Kao, H., Smith, B., Goerzen, C., Kontou, B., Dokht, R., Hutchinson, J., Tan, F., and Mahani, A. B. (2017). A comprehensive earthquake catalogue for the fort st. john–dawson creek region, british columbia.

Visser, R., Kao, H., Smith, B., Goerzen, C., Kontou, B., Dokht, R., Hutchinson, J., Tan, F., and Mahani, A. B. (2020). A comprehensive earthquake catalogue for the fort st. john-dawson creek region, british columbia, 2017-2018.

Wang, B., Harrington, R. M., Liu, Y., Kao, H., and Yu, H. (2019). Remote dynamic triggering of earthquakes in three unconventional canadian hydrocarbon regions based on a multiple-station matched-filter approachremote dynamic triggering of earthquakes in three unconventional canadian hydrocarbon regions. *Bulletin of the Seismological Society of America*, 109(1):372–386.

Wang, B., Harrington, R. M., Liu, Y., Yu, H., Carey, A., and van der Elst, N. J. (2015). Isolated cases of remote dynamic triggering in canada detected using cataloged earthquakes combined with a matched-filter approach. *Geophysical Research Letters*, 42(13):5187–5196.

Wang, R., Gu, Y. J., Schultz, R., Zhang, M., and Kim, A. (2017). Source characteristics and geological implications of the january 2016 induced earthquake swarm near crooked lake, alberta. *Geophysical Journal International*, 210(2):979–988.

Weber, B., Becker, J., Hanka, W., Heinloo, A., Hoffmann, M., Kraft, T., Pahlke, D., Reinhardt, J., and Thoms, H. (2007). Seiscomp3—automatic and interactive real time data processing. In *Geophysical Research Abstracts*, volume 9.

Yenier, E. (2017). A local magnitude relation for earthquakes in the western canada sedimentary basina local magnitude relation for earthquakes in the western canada sedimentary basin. *Bulletin of the Seismological Society of America*, 107(3):1421–1431.

Zheng, Y. (2018). Transient pressure surge in a fluid-filled fractureshort note. *Bulletin of the Seismological Society of America*, 108(3A):1481–1488.

Appendix A

Appendices

A.1 Selection criteria and parameters thresholds

Earthquake candidate selection thresholds:

Epicentral depth $\leq$ 100 km

Surface wave magnitude (M$_S$) $\geq$ 6.0

PGV$_m$ $\geq$ 100 μm/s

Multi-station matched-filter chosen parameters:

10x MAD threshold

0.4 CCC threshold

5-15 Hz bandpass filter

4 minimum phase picks

Statistical test thresholds for 95% confidence level:

$P \geq$ 0.975

$\gamma \geq$ 1.6

$\beta \geq$ 2.0

$Z \geq$ 2.0

Table A.1: Station locations and start times

Network	Station	Latitude	Longitude	Elevation (m)	Start time (UTC)
1E	MONT1	55.910149	-120.58654	697	2018-10-01T22:20:08
1E	MONT2	56.019718	-120.046967	642	2018-10-01T22:24:00
1E	MONT3	56.005779	-120.45388	783	2018-10-01T19:17:21
1E	MONT6	56.110291	-121.016991	650	2018-10-03T19:23:00
1E	MONT8	56.06731	-120.777428	695	2019-07-15T16:15:44
1E	MONT9	55.803902	-120.538757	832	2019-10-07T20:20:10
1E	MONTA	56.104321	-121.070038	651	2019-10-05T20:25:00
CN	NBC4	55.687279	-120.66024	815	2013-03-01T00:00:00
CN	NBC7	56.267792	-120.842621	676	2014-08-10T00:00:00
XL	MG01	56.05484	-120.637993	721	2017-06-19T03:12:26
XL	MG02	55.866791	-120.083992	642	2017-06-14T12:59:00
XL	MG03	55.912151	-120.44136	697	2017-06-16T19:40:00
XL	MG04	55.99136	-120.338043	682	2017-06-17T19:33:00
XL	MG05	55.895142	-120.301949	795	2017-06-15T21:15:00
XL	MG06	55.87212	-120.041481	639	2018-06-22T17:50:00
XL	MG07	55.783562	-120.40242	749	2017-08-02T17:30:00
XL	MG08	55.84116	-120.87307	722	2017-06-14T13:00:00
XL	MG09	55.74419	-120.779617	795	2017-06-18T20:53:40
XL	MG10	55.722851	-120.063347	798	2019-10-01T18:30:02
XL	RU01	56.145069	-120.480042	612	2019-07-30T13:49:49
XL	RU02	56.131989	-120.188187	611	2019-07-30T13:49:51
XL	RU03	55.807442	-121.134506	795	2019-09-26T18:35:00
XL	RU04	55.961369	-121.038788	892	2019-10-03T20:45:00
XL	RU05	56.180611	-120.733391	606	2019-10-04T19:27:41
XL	RU06	55.98959	-120.526909	773	2019-09-29T17:23:55

Table A.2: Earthquakes with measured peak ground velocities >100 μm/s for at least one of the radial (PGV_R), transverse (PGV_T), or vertical (PGV_Z) components of station NBC4. Event ID is tied to those of Table 2.1, with event origin times in UTC. Peak dynamic triggering stress (τ) is calculated from the component of highest measured peak ground velocity, and PGV_t is the theoretical peak ground velocity, for each event. Source area represents the approximate epicentral location. Events 7, 10, and 14 are excluded due to a lack of waveform data for those periods.

Event ID	Date	Origin time	Mag (M_W)	PGV_R (μm/s)	PGV_T (μm/s)	PGV_Z (μm/s)	PGV_t (μm/s)	τ (kPa)	Source area
1	2017-09-08	04:49:19	8.2	956	1167	878	898	13.10	Mexico
2	2018-01-10	02:51:33	7.5	208	231	197	165	2.59	Honduras
3	2018-01-23	09:31:40	7.9	538	1203	604	2547	13.51	Alaska
4	2018-10-22	05:39:39	6.5	25	160	31	277	1.80	Port Hardy
5	2018-10-22	06:16:26	6.8	72	452	84	555	5.08	Port Hardy
8	2018-12-20	17:01:55	7.2	91	304	85	135	3.4	Russia

Table A.3: Events detected during visual analysis of the October 22 2018 and January 28 2020 mainshocks. The first arrival times of each event are shown in UTC.

First arrival	Number of phase picks
2018-10-22T06:22:12	7
2020-01-28T18:38:12	13
2020-01-28T18:40:10	3
2020-01-28T19:48:01	3
2020-01-28T19:59:55	6
2020-01-28T20:25:17	6
2020-01-28T20:28:07	6
2020-01-28T20:47:29	6
2020-01-28T20:50:19	3
2020-01-28T20:53:53	4
2020-01-28T20:58:49	27
2020-01-28T21:14:20	7
2020-01-28T21:18:25	6
2020-01-28T21:23:08	10
2020-01-28T21:23:37	3
2020-01-28T21:24:02	8
2020-01-28T21:38:59	3
2020-01-28T22:51:51	3
2020-01-28T22:51:52	3
2020-01-28T23:05:55	3
2020-01-28T23:07:36	3